

Exploring electron spin dynamics in spin chains using defects as a quantum probe.

L. Soriano,^{1,*} A. Manoj-Kumar,¹ G. Gerbaud,² A. Savoyant,¹ R. Dassonneville,¹
H. Vezin,³ O. Jeannin,⁴ M. Orio,⁵ M. Fourmigué,⁴ and S. Bertaina^{1,†}

¹ CNRS, Aix-Marseille Université, Université de Toulon, IM2NP, Marseille, France.

² CNRS, Aix-Marseille Université, BIP, Marseille, France.

³ CNRS, Université de Lille, LASIRE, Villeneuve d'Ascq, France

⁴ Université de Rennes, CNRS, ISCR, F-35042 Rennes, France.

⁵ CNRS, Aix-Marseille Université, Centrale Marseille, ISM2, Marseille, France.

(Dated: December 9, 2025)

We investigate the quantum dynamics of the electron spin resonance of topological defects (edge state) in dimerized chains. These objects are discontinuities of the spin chain protected by the properties of the global system leading to a quantum many-body multiplet protected from the environment decoherence. Despite recent achievements in the realization of isolated and finite spin chains, the potential implementation in quantum devices needs the knowledge of the relaxation and decoherence sources. Our study reveals that electron spin lattice relaxation is governed at lowest temperatures by phonon-bottlenecked process and at high temperature by the chain dimerization gap. We show that the inter edge-state effective dipolar field is reduced by the intrachain exchange coupling leading to a longer coherence time than isolated ions at equivalent concentration. Ultimately, we demonstrate that the homogeneous broadening is governed by the intra-chain dipolar field, and we establish design principles for optimizing coherence in future materials.

I. INTRODUCTION

Topological quantum states in condensed matter systems represent a fascinating class of collective excitations whose properties are governed by global symmetries rather than local perturbations. A prime example is the $S=1/2$ topological defect, or "edge state", that emerges in gapped one-dimensional (1D) spin chains [1]. While their existence has been established for decades [2–5], a fundamental question remains unanswered: what are the intrinsic limits of their quantum coherence, and what physical mechanisms govern their interaction with the environment? Understanding these dynamics is essential both for fundamental physics—to reveal how many-body correlations influence decoherence—and for assessing the potential of such states in future quantum applications. This paper provides the first comprehensive experimental and theoretical study of the relaxation and decoherence dynamics of these topological edge states.

Similar effects are predicted in systems undergoing a Spin-Peierls transition systems which have a nonmagnetic ground state because of a dimerization of the spin and/or lattice [6–8]. Furthermore, because the influence of the spins located at the regular sites of the chains is greatly reduced, a thorough study of the defect-induced magnetic properties is possible with such a non-magnetic singlet ground state. From a theoretical perspective, defects in spin chains have attracted considerable interest in the context of quantum information science. Since Bose's pioneering proposal in 2003 [9], numerous theoretical studies have explored the possibility that defects in spin

chains could serve as qubits connected by spin-mediated interactions, potentially enabling quantum state transfer protocols [10–12]. While these proposals remain largely theoretical, recent experiments on artificial atomic chains [13] and quantum dots [14] have begun to explore related physics. A critical open question for any such application is: what limits the coherence time of embedded defects in real materials? Addressing this question requires a detailed understanding of the microscopic decoherence mechanisms, which has been lacking until now.

Magnetic properties of defects in cuprate spin chain like Sr_2CuO_3 [15] and CuGeO_3 [16] have been reported but no coherence was observed so far. Recently, a well-known class of systems, the organic spin chains with spin-Peierls ground state, has shown edge states with relatively long coherence times. Initially observed in $(\text{TMTTF})_2\text{PF}_6$ [17], the absence of spin echo has prevented the study of decoherence mechanisms. Among the large family of organic spin chains, one of them is of particular interest: *ortho*-dimethyltetraphiafulvalene or *o*-DMTTF. The serie of $(o\text{-DMTTF})_2\text{X}$ has been reported with centro-symmetric counter ions ($\text{X} = \text{Br}, \text{Cl}$ and I) [18–20]. While these materials show some conductivity at room temperature, they become insulators below about 150 K and undergo a spin-Peierls transition around $T_{\text{SP}} \simeq 50$ K. Their magnetic properties can be described by the spin-Peierls hamiltonian:

$$\mathcal{H} = \sum_i J(1+\delta) \mathbf{S}_{2i-1} \cdot \mathbf{S}_{2i} + J(1-\delta) \mathbf{S}_{2i} \cdot \mathbf{S}_{2i+1} \quad . \quad (1)$$

where J is the Heisenberg isotropic coupling, δ the dimerization parameter and \mathbf{S}_i a spin $S = 1/2$ at the site i . At high temperature (*i.e.* $T > 50$ K), $\delta = 0$ corresponds to the uniform spin chain while at low tem-

* Present address: CNRS, Institut Néel (UPR 2940), Grenoble, France.

† sylvain.bertaina@cnrs.fr

perature (*i.e.* below the spin Peierls transition temperature, T_{SP}) $\delta \neq 0$ corresponds to the dimerized spin chain with a non-magnetic ground state. J as well as δ has been reported using continuous wave EPR [20] : $J^{X=Br} = 600$ K, $J^{X=Cl} = 600$ K, $J^{X=I} = 670$ K, $\delta^{X=Br} = 0.08$, $\delta^{X=Cl} = 0.083$, and $\delta^{X=I} = 0.093$. Their highly one-dimensional character and the presence of a large spin gap in the bulk provide an ESR-silent background, allowing for an exceptionally clean probe of the in-gap edge states. Our study is performed below 20 K, so we consider that the spin-Peierls phase is fully stabilized. The presence of edge state is due to presence of imperfection in the crystal. In organic materials, this is mainly caused by electrochemical growth, which easily induces local breaks or stacking defects that cannot be corrected by annealing as in inorganic materials. Many numerical studies [4–8] have shown how these edge states can influence the overall behavior of the spin chain. In a finite chain, translational symmetry breaking will polarize the spins in the vicinity of the defect. Using computational methods such as Density Matrix Renormalization Group (DMRG), we can show that this spin polarization creates a spin cluster whose size (*i.e.* correlation length) depends on the dimerization parameter δ (see Figure S1).

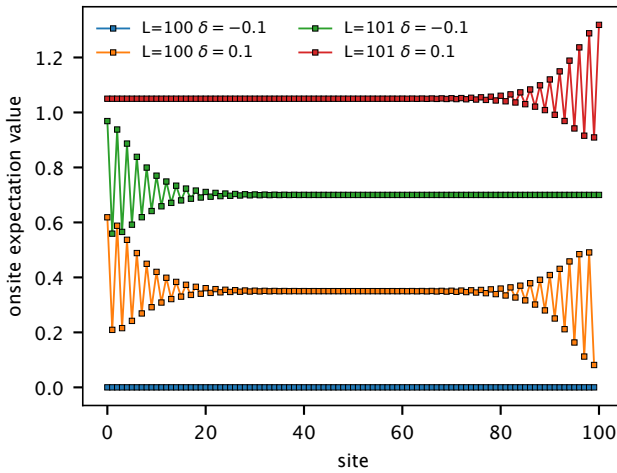


Figure 1. Local magnetization profiles obtained via DMRG simulations for open spin chains of length $L=100$ and $L=101$ spins. The simulations are performed using the spin-Peierls Hamiltonian (eq. (1)) with a dimerization parameter $\delta = \pm 0.08$. The different colored lines represent the expectation value of the S_z operator at each lattice site. The results illustrate how the open boundary conditions lead to a significant polarization of the spins at the chain ends, forming a cluster.

For $\delta = 0.08$ which is the estimated value for $(o\text{-DMTTF})_2X$ at low temperature [20] the local magnetization of an open spin chain with odd or even number of spins is given in Figure 1. The end of the chain has the effect of polarising many spins forming a cluster of connected spins to the rest of the chain. This object has a ground state $S=1/2$ [21] and is denoted in the literature as of pinned soliton [16, 17, 22], end chain [6, 23]

or edge state [24] and in the following it will be referred as quantum spin chain edge state (QSC-ES). Due to the topological protection in this many body system, intense effort have been devoted to create nanoscale individual QSC-ES [25–27] but the nature of decoherence and relaxation mechanism remain unclear.

In this article, we present a comprehensive study of relaxation and decoherence of QSC-ES of a quasi-1D spin chain embedded in 3D crystals. We have chosen the $(o\text{-DMTTF})_2X$ family because the bulk magnetic properties are well known [20, 21] with a large exchange $J \sim 600$ K and a dimerization parameter $\delta \sim 0.08$ which is neither too small as in $(TMTTF)_2X$ family ($\delta \sim 0.03$) [28] where very narrow homogeneous lines prevented echo observation in previous studies, nor too large like $BEDT\text{-TTF}$ [29] which would lead to overly localized, trivial defects. In the first part, we show that the spin lattice relaxation of QSD-EC is related the properties of the bulk spin chain. Then, the decoherence processes of QSD-EC are precisely studied. We demonstrate that the spin diffusion processes such as instantaneous and spectral diffusions are renormalized by the many body property of the topologically protected QSD-EC.

II. EXPERIMENTAL DETAILS

A. Crystals description.

Single crystals of $(o\text{-DMTTF})_2Br$, $(o\text{-DMTTF})_2Cl$, and $(o\text{-DMTTF})_2I$ were grown via electrocrystallization following the standard procedure described in Ref.[30]. The structural, electronic and magnetic characterizations were reported in Refs. [18, 30, 31]. Their crystallographic structures are shown in Figure 2. They all have tetragonal unit cell (space group $I\bar{4}2d$ (no. 122) [30]) with cell parameters $a = b = 16.93$ Å, 17.09 Å, 17.40 Å and $c = 7.040$ Å, 7.058 Å, 7.098 Å, respectively. The cell contains four pairs of molecules of $o\text{-DMTTF}$ which stack along the axis perpendicular to the plane of the molecules (c axis). Each pair of $o\text{-DMTTF}$ molecule is partially oxidized and shares one hole and so, one spin. Each stack is rotated by 90° with respect of the neighboring stacks. As a consequence, the interaction between spins along the stacking axis is very strong [18, 20, 30, 31] but the interaction between spin chains is very weak. The spin-Peierls transition has been reported in all three compounds with a dimerization temperature T_{SP} around 50 K. Within the temperature range examined in our study (< 20 K) the dimerized phase is fully stabilized.

These crystals have a needle-like shape with the chain axis along the long length of the needle. The largest crystals were used in the low-temperature electron spin resonance (ESR) study, where defect signals were observed but remained weak due to the low concentration of strongly correlated defects. The typical dimensions were $0.2 \times 0.2 \times 3$ mm³, the longest being the chain axis. To avoid the effects of temperature cycle history, a

III. SPIN LATTICE RELAXATION

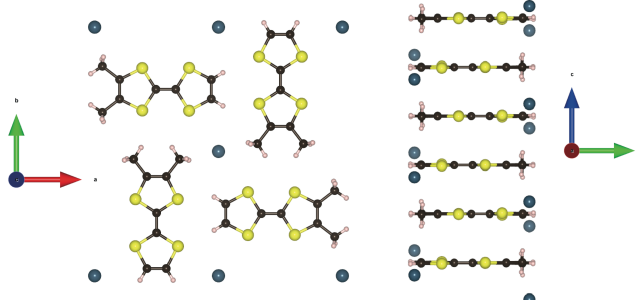


Figure 2. Crystal structures of $(o\text{-DMTTF})_2\text{Br}$, $(o\text{-DMTTF})_2\text{I}$ and $(o\text{-DMTTF})_2\text{Cl}$. The left panels show the unit cell viewed along the c axis, while the right panels show the packing along the a axis. The crystallographic axes are indicated with colored arrows (red, green, and blue for a , b , and c , respectively). The $o\text{-DMTTF}$ molecules form stacks along the c -axis, with strong intra-stack interactions leading to 1D magnetic behavior. The packing and interactions are slightly different due to the different counter-anion.

fresh sample was used for each series of measurements. The samples were glued to a suprasil quartz rod using a small amount of Apiezon grease on one side to minimize stress during temperature sweeps. The samples came from the same batches that the ones used for cw-ESR concentration obtained in [20] and this in order to avoid concentration difference between samples. Moreover, to be sure about the concentration we have re-performed a cw-ESR intensity measurements right after the ID study.

B. ESR spectrometer setup

Coherent spin dynamics were investigated using a pulsed X-band (9.4 GHz), Q-band (34GHz) and W-band (94GHz) ESR spectrometer (Bruker E580), equipped with an Oxford CF935 He-flow cryostat and a ColdEdge Stinger cryogen-free coldhead, allowing to reach a base temperature of 5.5 K at the sample position. The experiments were conducted using microwave cavities optimized for pulsed operation. We performed inversion recovery experiments ($\pi - t_1 - \pi/2 - \tau - \pi - \tau - \text{echo}$) for T_1 measurements, and used 2-pulse Hahn echo ($\pi/2 - \tau - \pi - \tau - \text{echo}$) and 3-pulse ($\pi/2 - \tau - \pi/2 - T_W - \pi/2 - \tau - \text{echo}$) stimulated echo sequences for T_2 measurements. The repetition rate was set in order to let the spin system fully relax.

The spin-lattice relaxation time, T_1 , represents the characteristic duration required for a spin to return to its equilibrium state after random flips along the spin quantization axis. Longitudinal relaxation T_1 imposes an intrinsic limit on the transverse relaxation T_2 , such that $T_2 \leq 2T_1$. Therefore, understanding the mechanisms of spin-lattice relaxation is crucial for understanding spin decoherence. In magnetically diluted systems, such as rare earth ions, transition metal ions or nitrogen vacancy (NV) centers, which represent the majority of the studies on electron spin qubit, the spin-flip induced by the spin-phonon interaction is well understood and can be divided in three processes (Fig. S2): The direct absorption or emission of a phonon resonating between the spin states $|a\rangle$ and $|b\rangle$. This process dominates at low temperature, when the density of phonon is mostly at the energy of the microwave $h\nu = \delta$. When the temperature increases, thermally assisted relaxation mechanism using two phonons is induced: The non resonant Raman process occurs by virtual absorption of a phonon of energy δ_1 and is followed by emission of a phonon of energy δ_2 and finally, the resonant Orbach process occurs through a third state $|c\rangle$. This last mechanism exists only if the Debye temperature θ_D is larger than the energy of the third state $|c\rangle$. For a Kramers ion, the spin-lattice relaxation time as a function of temperature is given by [32, 33]:

$$\frac{1}{T_1} = \alpha_D \cdot T + \alpha_{R5} \cdot T^5 + \alpha_{R7} \cdot T^7 + \alpha_{R9} \cdot T^9 + \alpha_O \cdot \Delta_0^3 \exp(-\Delta_0/k_B T) \quad (2)$$

where α_D is the direct absorption-emission process coefficient and is dependent to the external magnetic field as H_0^4 , α_{Ri} are the two-phonon Raman process coefficients such as α_{R5} describes mostly molecular systems, α_{R7} is proportional to H_0^2 , α_{R9} is the principal coefficient expected in Kramers ions, α_O is the resonant Orbach coefficient[34] with Δ_0 the gap with the first excited spin state.

In this section we study T_1 as function of the temperature between $T=5$ K and 20 K and as function of the magnetic field using three microwave frequencies 9.7 GHz (0.35 T), 34 GHz (1.21 T) and 94 GHz (3.35 T) using the inversion recovery pulse sequence: A π pulse inveres the population of spins, and after waiting for a time t_1 the recovered magnetization $\langle S_z \rangle$ is probed using a Hahn echo ($\pi - t_1 - \pi/2 - \tau - \pi - \tau - \text{echo}$). Examples of magnetization recovery at $T = 7$ K and 14.5 K are shown in Figure 3. While at high temperature, the recovery is clearly monoexponential, it deviates at low temperature and a stretched exponential is needed to fit the experimental values (eq.(3)).

$$\frac{M_0 - M_z(t)}{2} = \exp(-t/T_1^{\text{str}})^\beta \quad (3)$$

The variation of the stretched parameter β as function of temperature for the three frequencies used is shown for $(o\text{-DMTTF})_2\text{Br}$ in Figure 3 (c). At high temperature ($T > 13$ K), $\beta = 1$ indicates a uniform distribution of T_1 while below ($T < 13$ K), β progressively decreases with a minimum of 0.5 at $T = 5$ K. No significant effect of the microwave frequency, and consequently, of the magnetic field is observed.

The stretched exponential behavior of longitudinal magnetization has been observed in a wide variety of systems and research areas [35–37], and usually fits relaxation processes in disordered and quenched electronics. However the microscopic physical meaning of T_1^{str} when $\beta < 1$ is debatable. Johnston [38] has shown that the stretched exponential is the Laplace transform of the probability density $P(1/T_1, \beta)$ of $1/T_1$. Knowing β it is then possible to reconstruct $P(1/T_1, \beta)$ (see Figure S12 for some examples). It is worth to notice that the maximum of $P(1/T_1, \beta)$ is not T_1^{str} but Johnston has shown that in the case of $0.5 < \beta < 1$, $1/T_1^{\text{str}}$ can be described as the median of $P(1/T_1, \beta)$. Thus, while the temperature dependence of T_1^{str} has a physical significance, extracting and interpreting quantitative prefactors could be hazardous.

Now, we examine the temperature dependence of $1/T_1^{\text{str}}$. Using the case of $(o\text{-DMTTF})_2\text{Br}$, Figure 4 illustrates the temperature dependence of $1/T_1^{\text{str}}$ in log-log scale for the three microwave frequencies available. The dashed line is the best fit for the low temperature part ($T \lesssim 11$ K) using the direct one-phonon process ($\alpha_D \cdot T$) which is assumed to be dominant in this range of temperature. Clearly the fit is poor and it is evident that the relaxation rates T_1^{str} do not exhibit linear temperature dependence. This observation holds true for $(o\text{-DMTTF})_2\text{Cl}$ (Fig. S5), and $(o\text{-DMTTF})_2\text{I}$ (Fig. S6) as well. A much better fit was found using a square temperature dependence of $1/T_1^{\text{str}}$ using $\alpha_B \cdot T^2$ (black lines in Fig. 4). The magnetic field dependence of the spin-lattice relaxation does not follow the usual behaviour of the direct regime. In fact, in a Kramers doublet, such as in our case, we would expect a dependence in H_0^4 and therefore a variation of 4 orders of magnitude between the X-band and W-band measurements, which is clearly not the case. Here, the low-temperature behaviour is rather linear with the magnetic field.

The linear field dependence and the quadratic temperature dependence of $1/T_1^{\text{str}}$ suggest that the direct process is "bottlenecked". Indeed, in the direct-phonon process, it is assumed that the phonon emitted during the relaxation is rapidly absorbed by the thermal bath. However, if the phonon remains long enough in the crystal, it might be re-absorbed by the spin system, reducing the relaxation efficiency. The phonon-bottleneck was predicted by van Vleck [39] and observed in various systems. The

relaxation rate in a phonon-bottlenecked direct process is approximated by [32, 40]:

$$\frac{1}{T_1^{\text{phb}}} = \frac{3\omega^2\Delta\omega}{2\pi^2v^3n\tau_{\text{ph}}} \coth^2\left(\frac{\hbar\omega}{2k_B T}\right) \quad (4)$$

where v the velocity of sound in the crystal, $\Delta\omega$ is the resonance linewidth, n is the concentration of spins, and τ_{ph} is the lattice-Åbath relaxation time. Assuming $k_B T \gg \hbar\omega$, and the inhomogenous linewidth is field dependent we can simplify eq.4 by

$$\frac{1}{T_1^{\text{phb}}} = \alpha'_B H_0 T^2 \quad (5)$$

It has been observed that the phonon-bottleneck process of the spin lattice relaxation is accompanied by a non-exponential decay of the magnetization [41] (see eq.(3)) which is a behavior we also observed at low temperature. We can conclude that the temperature dependence of the stretched parameter β is the signature of the phonon-bottleneck process that takes place below about 13 K (see Fig. 3(c)).

Having identified the low-temperature phonon-bottlenecked direct process, we now focus on the behavior at higher temperature. To study the two-phonon regimes, we have subtracted the low-temperature behavior from the total relaxation : $1/T_1^{\text{HT}} = 1/T_1 - \alpha_B T^2$. Since the Orbach- and Raman-processes are highly non-linear, we present in Figure 5 the temperature dependence of the corrected relaxation either as (i) $\log(1/T_1^{\text{HT}})$ vs $1/T$ or (ii) $\log(1/T_1^{\text{HT}})$ vs $\log(T)$. In the first case (i) the Orbach (resonant) process is linear with respect of the inverse of temperature while in the second case (ii), the Raman (non-resonant) process is linear in the log-log scale with the slope corresponding to the exponent (see eq. (2)).

The best fit using pure Orbach : $1/T_1 = \alpha_O \Delta_0^3 \exp(-\Delta_0/k_B T)$ and pure Raman : $1/T_1 = \alpha_{R9} T^9$ shows two different groups of systems. $(o\text{-DMTTF})_2\text{Cl}$ and $(o\text{-DMTTF})_2\text{Br}$ exhibit an Orbach process while $(o\text{-DMTTF})_2\text{I}$ has Raman- T^9 process. We think that these two different relaxation behaviors are directly related to the relative value of the spin-triplet gap. In the cases of $(o\text{-DMTTF})_2\text{Cl}$ and $(o\text{-DMTTF})_2\text{Br}$, the Orbach gaps Δ_0 obtained from the best fit of the temperature dependence of T_1 (Fig. 5) is coherent with the value of the spin-triplet gap Δ_{SP} . However, in the case of $(o\text{-DMTTF})_2\text{I}$, Δ_{SP} is large and no Orbach process is observed suggesting that no phonon has the energy to reach the triplet state (i.e. $\theta_D > \Delta_{\text{SP}}$). Summary of the results for the three compounds and the accessible frequencies is reported in Table I.

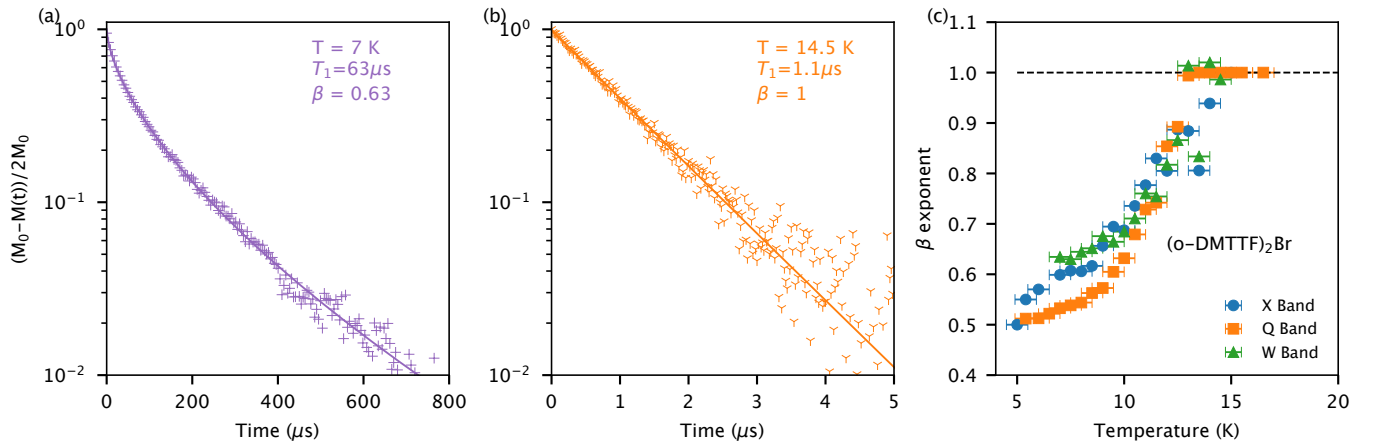


Figure 3. (a)-(b) Longitudinal magnetization as function of time after the inversion pulse. The semi-log scale is used to highlight the deviation from the monoexponential decay. The solid line is the best fit using eq. (3). (a) At $T = 7\text{ K}$, the stretched exponential parameter is $\beta = 0.65$ and (b) at $T = 14.5\text{ K}$ $\beta = 1$. (c) Temperature dependence of β for $(o\text{-DMTTF})_2\text{Br}$ and for the three microwave bands used.

Table I. Fitted parameters of spin lattice relaxation. $\alpha_B = \alpha'_B H_0$ (see (5)) is the direct-bottleneck α_{R9} the Raman and α_O the Orbach coefficients. The fit error estimation is included in the last digit.

	Band	α_B ($\text{s}^{-1}\text{K}^{-2}$)	α_{R9} $\times 10^{-6}(\text{s}^{-1}\text{K}^{-9})$	α_O $\times 10^4(\text{s}^{-1}\text{K}^{-3})$	Δ_0 (K)	Δ_{SP} [20, 31] (K)
$(o\text{-DMTTF})_2\text{Cl}$	X	68	-	1.1	147	178
	Q	350	-	1.1	138	178
$(o\text{-DMTTF})_2\text{Br}$	X	49.1	-	1.4	181	181
	Q	94.6	-	1.4	170	181
	W	336	-	1.4	165	181
$(o\text{-DMTTF})_2\text{I}$	X	88.8	4.17	-	-	230
	Q	157	4.17	-	-	230
	W	676	4.17	-	-	230

IV. ELECTRONIC SPIN COHERENCE TIME

In this part, we focus on the electronic coherence time T_2 and the mechanisms of decoherence of $(o\text{-DMTTF})_2\text{I}$, $(o\text{-DMTTF})_2\text{Br}$ and $(o\text{-DMTTF})_2\text{Cl}$. Several phenomena contribute to the loss of coherence of electronic spins. Firstly, the spin-lattice relaxation resulting from spin-phonon interactions sets the physical limit for the coherence time, *i.e.*, $T_2 < 2T_1$. We have discussed the various relaxation mechanisms in detail in section III and identified which ones were involved in the relaxation of $(o\text{-DMTTF})_2X$. This limit is rarely reached because the excited spins are subject to random dephasing caused by spin-spin interactions. These dephasing processes contribute to reducing the coherence time T_2 and are collectively represented by the term Γ_ϕ . The coherence time is then related to the relaxation time T_1 by the relation:

$$\frac{1}{T_2} = \Gamma_\phi + \frac{1}{2T_1} \quad (6)$$

Let us note that the term Γ_ϕ is a sum of different contributions to the random phase shifts. Some contributions to the phase shifts are intrinsic, such as the flip-flop process, while others are due to the environment and may depend on the measurement method, such as spectral diffusion [42] and instantaneous spectral diffusion [43, 44]. Therefore, the coherence time value depends on the measurement method. These various decoherence mechanisms have been detailed in [45].

We employ both two-pulse Hahn echo (2PE) and three-pulse stimulated echo (3PE) to clarify the dynamic interactions that give rise to spin diffusion (SD) in QSC-ES ensembles. In this context, the 2PE involves flipping the spins into the transverse plane with a $\pi/2$ pulse. The spins defocus for a time τ , and then we refocus them with a pulse corresponding to an angle θ_2 (usually optimum for $\theta_2 = \pi$), the total sequence being $\frac{\pi}{2} - \tau - \pi - \tau - \text{echo}$. The 3PE splits the refocusing π pulse into two $\frac{\pi}{2}$ pulses separated by a time T_W : $\frac{\pi}{2} - \tau - \frac{\pi}{2} - T_W - \frac{\pi}{2} - \tau - \text{echo}$. The 2PE and 3PE sequences were first used by Mims *et al.* [42] and since then the underlying theory was im-

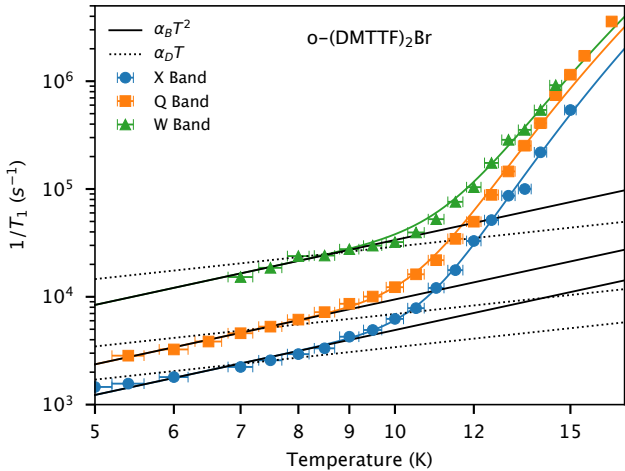


Figure 4. Temperature dependence of the inverse stretched relaxation time ($1/T_1^{\text{str}}$) for $(o\text{-DMTTF})_2\text{Br}$, obtained via inversion recovery experiments at three microwave frequencies: X-band (9.7 GHz), Q-band (34 GHz), and W-band (94 GHz). The data are plotted on a log-log scale. Dashed lines represent fits to a linear temperature dependence ($\alpha_D T$), reflecting the direct phonon process, which provides a poor fit. Black solid lines show fits to a square of temperature dependence ($\alpha_B T^2$), indicative of a possible phonon bottleneck effect.

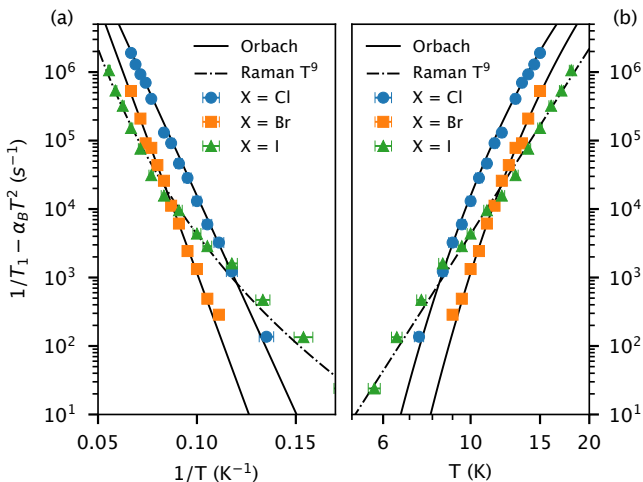


Figure 5. Temperature dependence of the spin lattice relaxation rate corrected by the phonon bottleneck contribution with respect to (a) $1/T$ or (b) T in log-scale. Plain and dash-dotted lines are the best fit using Orbach and Raman model respectively.

proved using uncorrelated-sudden-jump [46, 47]:

$$I_E(2\tau + T_W) = V_{\text{ESEEM}} I_0 \exp(-2\pi\Gamma_{\text{eff}}\tau) \exp\left(-\frac{T_W}{T_1}\right)^\beta \quad (7)$$

$$\Gamma_{\text{eff}} = \Gamma_0 + \frac{\Gamma_{\text{SD}}}{2} \{R\tau + 1 - \exp(-RT_W)\} \quad (8)$$

where I_0 is the echo amplitude at zero delay, and V_{ESEEM} represents to the electron spin echo envelope modulation (ESEEM) caused by the magnetic dipole-dipole interaction of the QSC-ED and the nuclear spins in $(o\text{-DMTTF})_2X$ [48]. ESEEM from the host nuclear spins such as ^1H , ^{13}C and counter-ions was not observed. This absence of signal will be discussed after. T_1 is the spin-lattice relaxation and we have added β to take into account the phonon-bottleneck effect presented before. Eq. (7) and (8) are valid when $\tau \ll T_1$.

The effective decaying rate Γ_{eff} incorporates the coefficients Γ_0 , Γ_{SD} and R . The coefficient Γ_0 characterizes decoherence processes fast enough compared to the timescale of the measurements and also the instantaneous diffusion induced by the microwave excitation pulses. Γ_{SD} and R describe the spectral diffusion during the delays τ and T_W . Specifically, R denotes the average spin-flip rate, while Γ_{SD} represents the full width at half maximum (FWHM) contribution to the dynamic distribution of transition frequencies.

In the case of $T_W = 0$ the sequence corresponds to the 2PE.

$$I(2\tau) = I_0 \exp\left(-2\pi\Gamma_0\tau - 2\pi\frac{\Gamma_{\text{SD}}R}{2}\tau^2\right) \quad (9)$$

$$= I_0 \exp\left(-\left(\frac{2\tau}{T_2}\right)^n\right) \quad (10)$$

In the presence of pure spectral spin diffusion caused by non resonant spin bath (nuclear or electronic), the decay is expected to be a stretched exponential with n ranging between 2 and 3 [42, 43, 49]. A comprehensive derivation as well as validity questions can be found in Ref. [50].

Instantaneous diffusion

Instantaneous diffusion (ID) is a decoherence mechanism caused by the microwave excitations used to refocalize the spins that generate a spin echo. During a π refocusing pulse, spin populations are inverted, altering the quantum state m_s of the resonant spins, and the locally perceived field for the spins is abruptly changed. The dephasing generated by ID is related to the coherence time by eq.(11):

$$\frac{1}{T_2} = \pi\Gamma_{0, ID} + \pi\Gamma_{ID} \langle \sin^2 \theta_2/2 \rangle_f \quad (11)$$

where the phase shift term Γ_{ID} of eq.(12) is proportional to the spin concentration and $\Gamma_{0, ID}$ is the decoherence

in absence of ID such as homogeneous broadening and spectral diffusion (SD).

$$\Gamma_{ID} = \frac{\mu_0 g^2 C \mu_B^2}{9\sqrt{3}\hbar} \quad (12)$$

A key characteristic is the angle of rotation of the refocalsation pulse θ_2 [51, 52] through the expression $\langle \sin^2 \theta_2/2 \rangle_f$, which describes the average probability of inverting all spins. It depends on various parameters such as the microwave field (proportional to the Rabi frequency ν_R) and the profile f of the ESR line (a lorentzian of half width at half maximum $\Delta H_{1/2}$ in our case):

$$\langle \sin^2 \theta_2/2 \rangle_f = \int_{-\infty}^{+\infty} \frac{\nu_R^2}{\nu_R^2 + \eta^2} \sin^2 \left(\frac{\theta_2}{2} \sqrt{1 + \frac{\eta^2}{\nu_R^2}} \right) f(\eta + \Delta) d\eta \quad (13)$$

When $\langle \sin^2 \theta_2/2 \rangle_f = 1$, all spins involved in the ESR line are excited. However, in our case the effect of a partially excited line has to be taken into account. As an example let's consider (*o*-DMTTF)₂I where $\nu_R = 10.5$ MHz and $\Delta H_{1/2} = 2.5$ G ($\equiv 7$ MHz). With our parameters, $\langle \sin^2 \theta_2/2 \rangle_f = 0.56$ for a total refocusing pulse $\theta_2 = 180\text{}\text{\AA}$. This situation occurs when the microwave power is not sufficient to excite all spins constituting the inhomogeneous line.

To observe the effect of ID on the electronic coherence time, we measured the decay of the Hahn echo using eq. (10) and we varied the refocusing angle θ_2 using the sequence: $\frac{\pi}{2} - \tau - \theta_2 - \tau - \text{echo}$. Figure 6 shows the decay time T_2^{-1} of (*o*-DMTTF)₂I at $T = 5.4$ K. The inset displays two examples of Hahn echo decay with $\theta_2 = \pi/4$ (blue square) and $\theta_2 = \pi$ (orange circles). In all our measurements using 2PE, the stretched parameter n in eq.(10) was close to 1 showing that ID plays an important role in the decay time. It is also important to mention that the fits using eq.(9) were not satisfying since the relative weight of $\Gamma_{SD}R$ was small compared to Γ_0 . The decay times T_2^{-1} of the 2PE Hahn echo decay as a function of θ_2 and $\langle \sin^2 \theta_2/2 \rangle_f$ are presented in Figure 6(a) and (b) respectively. Using Eq.(11), we extract from the slope of Figure 6(b) $\pi\Gamma_{ID} = 294$ kHz, which leads to a concentration $C = 3.5 \times 10^{17}$ cm⁻³. The values of $\pi\Gamma_{0, ID}$, $\pi\Gamma_{ID}$, and C for (*o*-DMTTF)₂I, (*o*-DMTTF)₂Br, and (*o*-DMTTF)₂Cl are provided in Table II and compared to values extracted from continuous wave (cw) ESR measurements [20, 31].

For all compounds, the concentration obtained from ID is significantly lower than that determined by continuous wave electron spin resonance (cw-ESR). The concentrations from cw-ESR were derived by comparing the relative intensities of the spin chain and end chain signals, resulting in a very small error. In the case of ID, the fitting procedure is detailed in the Supplementary Information (SI) (Fig. S8, S9, S7, S10), with a cumulative error of

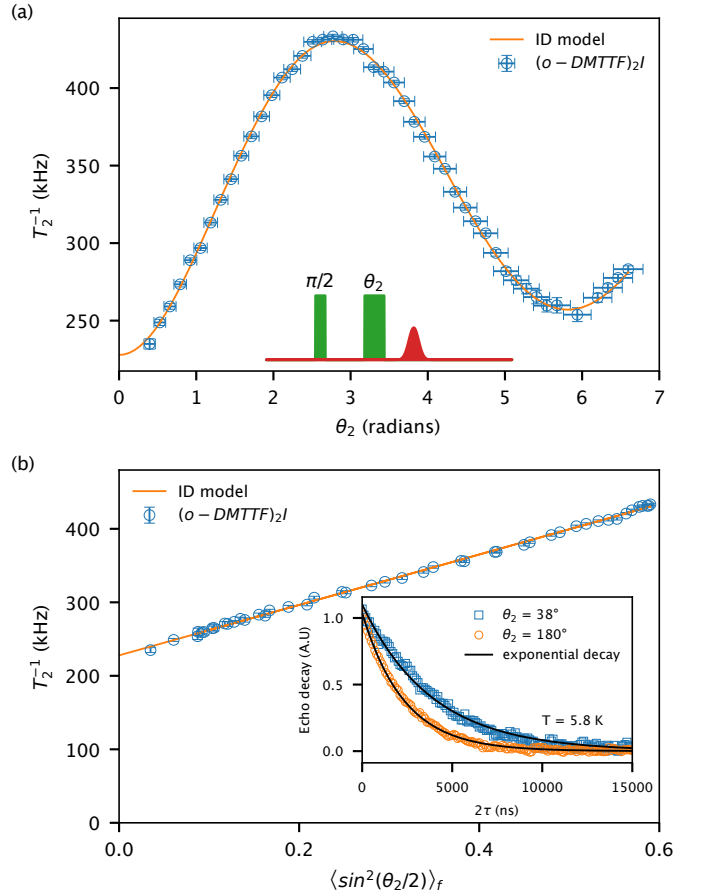


Figure 6. Effect of instantaneous diffusion on electronic coherence time T_2 measured by Hahn echo sequence of (*o*-DMTTF)₂I, $T = 5.8$ K, $H_0 \parallel c$ and in X band. (a) Plot of $1/T_2$ as a function of refocusing angle θ_2 and (b) as a function of $\langle \sin^2 \theta_2/2 \rangle_f$ where θ_2 is rotation angle of the second pulse in the sequence $\frac{\pi}{2} - \tau - \theta_2 - \tau - \text{echo}$. Plain lines correspond to the fit of experimental data using eq.(11).

less than 20%. The measurement error alone cannot account for the discrepancy in concentration resulting from the ID and cw-ESR studies. This discrepancy is a key finding of our work. For an ensemble of localized S=1/2 defects, the local spin concentration probed by dipolar interactions is expected to be equal than the average concentration ($C_{ID} = C_{cw}$). Our observation of $C_{ID} < C_{cw}$ strongly contradicts the localized spin model. It is important to note that the concentration from cw-ESR is directly related to the number of S=1/2 spins, whereas the concentration from ID is extracted from the effective dipolar field. The nature of the defect in quantum spin chains is fundamentally different than that of isolated defects (such as metallic ions or free radicals). As explained in the introduction and in Ref. [4-8], the spin S=1/2 we observed is made of dozens of coupled spins (see Figs. 1 and S1). It is not surprising that the strong correlation inside the spin chain might have an effect on the external couplings. To support this hypothesis, we performed

Table II. Fitted parameters of instantaneous diffusion ($\pi\Gamma_{0,ID}$, $\pi\Gamma_{ID}$) (see Fig. 6 and details in the main text). C_{ID} is the concentration extracted from eq.(12) and C_{cw} is the concentration obtained by cw-ESR measurements. The fit error estimation is included in the last digit.

	$\pi\Gamma_{0,ID}$ (ms^{-1})	$\pi\Gamma_{ID}$ (ms^{-1})	C_{ID} $10^{17} \cdot \text{cm}^{-3}$	C_{cw} [20] $10^{17} \cdot \text{cm}^{-3}$
(<i>o</i> -DMTTF) ₂ Cl	460	236	2.8	11
(<i>o</i> -DMTTF) ₂ Br	304	309	3.7	13
(<i>o</i> -DMTTF) ₂ I	208	294	3.5	8

DMRG calculation on two QSC-ES interacting though an Ising-like dipolar interaction $d\mathbf{S}_1^z \cdot \mathbf{S}_2^z$. We then calculated the anisotropic gap Δ_δ induced by d for many values of the dimerization factor δ and compared them with the anisotropic gap of 2 isolated spin Δ_{iso} . The details of calculation are presented in SI, and the main results are: For $\delta = 1$ (*i.e.* chain of non interacting dimers with a isolated spin at the end), $\Delta_{\delta=1} = \Delta_{iso}$, and when δ decreases, the gap Δ_δ reduces and reach zero for $\delta = 0$ (*i.e.* the uniform spin chain). In the particular cases of δ ranging from 0.08 to 0.096 for (*o*-DMTTF)₂X [20], we obtain $\Delta_{\delta=0.08} = 0.29\Delta_{iso}$ to $\Delta_{\delta=0.096} = 0.35\Delta_{iso}$ which match with the reduction of the effective concentration observed by ID. Although this model is very simple, it allows us to semi quantitatively explain the reduction in the effective dipole field between 2 QSC-ES. This result can be interpreted as follows: QSC-ES are many-body objects and it is therefore expected that the strong internal correlations arising from the isotropic J exchange interaction reduce the effect of dipole interactions.

Spectral Diffusion

Now ID has been quantified in all (*o*-DMTTF)₂X samples, we focus on other sources of decoherence such as homogeneous broadening and spectral diffusion (SD). 2PE and 3PE are complementary methods to extract coherence contributions. 2PE cannot separate the linewidth of the spectral diffusion Γ_{SD} and the spin-flip rate R (see. eq.(9)). Moreover, 2PE sequence is accurate to extract spectral diffusion when the stretch exponent n in eq.(10) is close to 2 while in our case it falls in the range 1 to 1.1. As a consequence, we have first studied the 3PE sequence at the lowest temperature. We measured the decay of the stimulated echo while increasing T_W at a constant τ value and we have then varied τ over the range of 200 ns to 4000 ns. This gives us a series of echo decays that we fitted simultaneously using eq.(7) and eq.(8). Selected stimulated echo decays for (*o*-DMTTF)₂I are presented in Figure 7.

The extracted values of the spin-lattice relaxation T_1^{-1} are coherent with the ones obtained by inversion recov-

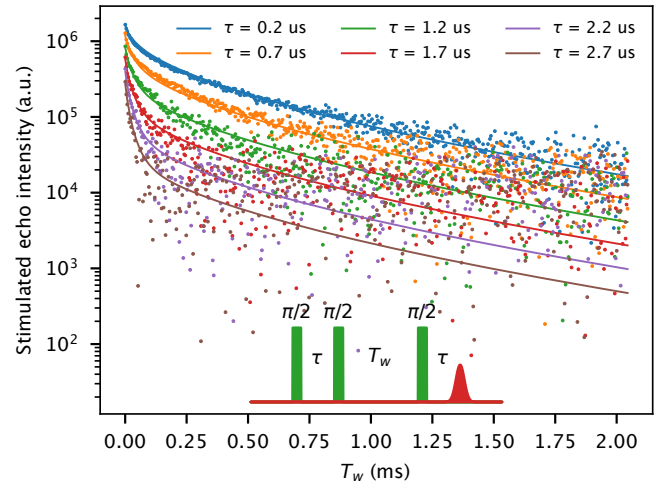


Figure 7. 3PE measurements probing spin coherence dynamics in (*o*-DMTTF)₂I at 6 K. The figure displays selected echo decay curves measured at various values of the delay time T_W . The decrease in signal intensity while increasing T_W is attributed to spectral diffusion, homogeneous broadening and spin-lattice relaxation effects. The solid lines correspond to simultaneous fits of the entire set of 3PE data using equations (7) and (8). The shared fit parameters Γ_0 , Γ_{SD} , R , T_1 and β are reported in Table III for I, Br and Cl.

Table III. Fitted parameters of spectral diffusion ($\pi\Gamma_0$, $\pi\Gamma_{SD}$, R , T_1^{-1} and β) obtained from the stimulated echo decay measurements. For comparison, $T_{1,IR}^{-1}$ and β_{IR} from inversion recovery measurements are also provided. The fit error estimation is included in the last digit.

X	Γ_0 (kHz)	Γ_{SD} (kHz)	R (kHz)	T_1^{-1} (kHz)	β	$T_{1,IR}^{-1}$ (kHz)	β_{IR}
Cl	130	150	20	2.5	0.59	2.4	0.55
Br	110	120	27	2.0	0.5	1.8	0.56
I	106	190	29.8	3.1	0.56	3.2	0.68

ery $T_{1,IR}^{-1}$. The values of the stretched exponents obtained from 3PE (eq. (9)) and inversion recovery (eq. (3)) are comparable, showing that the phonon-bottleneck process is visible also in 3PE. The values of Γ_{SD} agree with the dipolar interactions between QSC-ES. Values of the flipping rate R are one order of magnitude larger than what is expected for T_1 spin flipping only. If we take into account the flip-flop process into the flipping rate (see S4) we obtain a total spin flip rate of $R = 24$ kHz close to our experimental value. Finally, we note that the homogeneous linewidth Γ_0 is large compared to values reported in literature for equivalent spin concentration [47, 53, 54].

Now, let's compare the spin diffusion parameters obtained by 3PE with the temperature dependence of the 2PE decay. For this study, we performed a 2PE decay as function of temperature and we extracted the

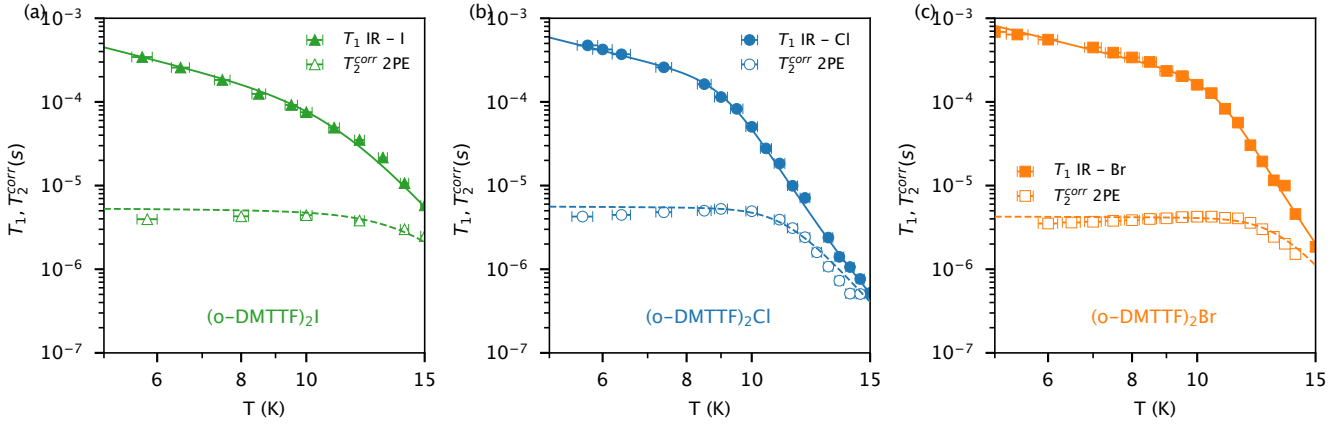


Figure 8. Temperature dependence of the corrected coherence time T_{2-2PE}^{corr} (open symbols) and spin-lattice relaxation time T_1 (solid symbols) for $(o\text{-DMTTF})_2X$ compounds ($X = \text{Cl}, \text{Br}, \text{I}$). The solid lines represent the phonon-bottleneck direct process and the high-temperature Raman or Orbach processes, as discussed in the main text. The dashed lines show the theoretical prediction of the coherence time using the parameters extracted from spectral diffusion analysis (see Table III), with no additional fitting parameters. The data demonstrate the interplay between spin-lattice relaxation and spectral diffusion in determining the coherence time of QSC-ES.

decoherence time T_{2-2PE} using eq. (10). We removed the ID contribution using the relation: $T_{2-2PE}^{-1\text{corr}} = T_{2-2PE}^{-1} - \pi\Gamma_{ID} \langle \sin^2 \pi/2 \rangle_f$. Corrected 2PE coherence time $T_{2-2PE}^{-1\text{corr}}$ and spin lattice relaxation time T_1 are provided in Figure 8 for $(o\text{-DMTTF})_2\text{I}$, $(o\text{-DMTTF})_2\text{Cl}$ and $(o\text{-DMTTF})_2\text{Br}$. The solid lines are the relaxation time using phonon bottleneck direct process and Raman or Orbach process as discussed previously. For the dashed lines we used the definition of the coherence time [43]:

$$T_2 = \frac{-a + \sqrt{a^2 + 2b/\pi}}{b} \quad (14)$$

where $a = \Gamma_0$, and $b = \Gamma_{SD}R/2$ are taken from Table III. This equation is valid for $T_2 \ll T_1$. To take into account the high temperature regime, we also include the limit due to spin lattice relaxation (see eq.(6)). It is important to note that no free fit parameters were used to simulate the dashed lines in Fig. 8. In the absence of fit parameters, our data describe accurately the temperature dependence of the 2PE. However it appears that T_{2-2PE}^{corr} is weakly sensitive to the diffusive part $\Gamma_{SD}R$ and the decoherence is mainly due to the homogeneous linewidth Γ_0 which explains why we did not extract accurately the spin diffusion contribution from 2PE.

The microscopic origin of Γ_0 remains an open question. The presence of nuclear spins in $(o\text{-DMTTF})_2X$ is not negligible, and in similar molecular magnets with an $S = 1/2$ ground state, such as V15 [55] and Cr7Ni [56], they are the primary source of decoherence, often exhibiting a significant ESEEM signature. However, in our study, no ESEEM signal from the systems was detectable, and previous work has shown that the hyperfine interactions in QSC-ED are significantly reduced by the

exchange coupling within the spin chain [21].

Another possibility arises from the decoherence effect of the spins within the chain. Although we are probing QSC-ED, which display a low concentration, they are composed of dozens of spins (see Figs. 1, S1) strongly correlated to the spin chain. In such magnets, the homogeneous linewidth can be estimated using the theory of moments. Introduced by Anderson and Weiss [57] this method shows that the linewidth is proportional to $\sum_i \frac{M_2^i}{J}$ where M_2^i is the second order moment of the interaction involved in the broadening such as electron-nuclear / electron-electron dipole interactions and anisotropic super-exchange interaction. Although this method is fairly simplistic regarding of the structure of QSC-ED, it does allow us to estimate the contribution of each interaction and their influence on the linewidth. To estimate the electro-nuclear dipolar field, DFT calculations were performed on a single molecule of $(o\text{-DMTTF})_2\text{I}$ and have shown a electro-nuclear dipolar field of $M_2^{e-n} \sim 10^{13} \text{ Hz}^2$ (see SI). The dipolar interaction caused by all the spins inside the chains give $M_2^{e-e} \simeq 3 \times 10^{17} \text{ Hz}^2$ and anisotropic exchange term although very small is estimated to $M_2^{ani} \simeq 3 \times 10^{16} \text{ Hz}^2$ (see S5). Finally, using the estimation of $J \sim 600 \text{ K}$ obtained in [20, 31] we obtain an homogenous intrinsic linewidth $\Gamma_h \sim 25 \text{ kHz}$ compatible with values reported in table III. Our method for estimating the sources of decoherence can be applied to other systems, in particular inorganic materials which were intensively studied in the 90s. As an example, let's confront the method to CuGeO₃ doped Zn [16]. While M_2^{e-n} and M_2^{e-e} remain weak, with $\Delta g \sim 0.1$ and $J \sim 100 \text{ K}$ we obtain $M_2^{ani} \simeq 5 \times 10^{20} \text{ Hz}^2$ and an homogeneous coherence time of 1ns which explain why no coherence was reported in

such material.

Design principles for optimizing coherence.—Our analysis provides actionable guidelines for engineering longer coherence times in quantum spin chain edge states. The key control parameter is the dimerization factor δ : according to our DMRG calculations (Fig. S2), the effective dipolar coupling between edge states scales approximately as $d_{\text{eff}}/d \approx 3\delta$ for small δ . This suggests that materials with weaker dimerization will exhibit reduced instantaneous diffusion and longer T_2 . However, reducing δ also increases the spatial extent of the edge state wavefunction (Fig. 1, S1), which may enhance homogeneous decoherence from intra-chain dipolar interactions. The optimal coherence is therefore expected at an intermediate δ value that balances these competing effects. For (o-DMTTF)₂X with $\delta \approx 0.08$ –0.09, our data suggest that homogeneous broadening ($\Gamma_0 \sim 100$ –130 kHz, Table III) currently limits T_2 , while instantaneous diffusion contributes comparably. To extend coherence beyond the microsecond regime achieved here, future materials design should target: (i) increased exchange coupling J to further suppress the homogeneous linewidth via exchange narrowing, (ii) reduced proton density through deuteration to minimize residual nuclear contributions, and (iii) optimization of δ near 0.05–0.08 to balance spectral diffusion suppression against wavefunction delocalization.

V. CONCLUSION

In summary, we have presented a comprehensive study of the quantum dynamics of quantum spin chain edge states using pulsed electron spin resonance. While pioneering ESR studies in the 1990s confirmed the existence of such topological states, the mechanisms governing their coherent dynamics have remained unexplored until now.

Our key findings are threefold. First, the spin-lattice relaxation of the edge state is intimately connected to the bulk properties of the spin chain: at high temperatures, relaxation proceeds via an Orbach process through the spin-Peierls gap Δ_{SP} (when $\Delta_{\text{SP}} < \theta_D$), while at low temperatures a phonon-bottleneck regime dominates regardless of the counter-ion.

Second, we have identified and quantified all sources of decoherence. Our central result is that the dipolar fields—both electronic and nuclear—which typically

dominate decoherence in dilute paramagnetic systems, are significantly renormalized by the intra-chain exchange coupling. This reveals the intrinsically many-body nature of the QSC-ES.

Third, DMRG calculations establish that the dimerisation factor δ is the key parameter controlling this renormalization: for large δ the edge state behaves as an isolated spin, while for small δ the effective inter-defect dipolar coupling is strongly suppressed. This framework quantitatively explains the long-standing puzzle of absent spin echoes in the (TMTTF)₂X family ($\delta \sim 0.03$), where dipolar-driven spectral diffusion is so weak that only homogeneous decoherence remains.

Our results provide concrete guidelines for materials optimization: (i) smaller δ values lead to reduced instantaneous diffusion, (ii) larger exchange coupling J reduces the homogeneous linewidth, and (iii) larger spin-Peierls gaps Δ_{SP} extend T_1 at intermediate temperatures. We emphasize that demonstrating functional quantum devices based on these principles—such as two-qubit gates or quantum sensing protocols—remains an important challenge for future work, requiring advances in materials synthesis and nanoscale addressability.

Nevertheless, this study establishes the foundational understanding necessary for such developments. In particular, our findings are directly relevant to the recent realization of topological edge states in atomically precise nanographene structures [25–27], where the internal dipolar field may constitute the ultimate limit to quantum decoherence. More broadly, this work demonstrates that many-body correlations in topological systems can provide an intrinsic protection mechanism against environmental decoherence—a principle that may extend to other classes of correlated quantum matter.

ACKNOWLEDGMENTS

This work is supported by Agence Nationale de la Recherche (ANR project à ÄJDySCORDE à Ä, ANR-20-CE29-0011). Financial support from the IR INFRANALYTICS FR2054 for conducting the research is gratefully acknowledged. A.M.K. is supported by ANR QuantEdu-France (22-CMAS-0001) and by France 2030 investment plan, as part of the Initiative à Ä Excellence à Ä Aix-Marseille Université à Ä A* MIDEX (AMX-22-RE-AB-199).

[1] H. Alloul, J. Bobroff, M. Gabay, and P. J. Hirschfeld, *Rev. Mod. Phys.* **81**, 45 (2009).

[2] S. Eggert and I. Affleck, *Phys. Rev. B* **46**, 10866 (1992).

[3] S. Eggert, I. Affleck, and M. Takahashi, *Phys. Rev. Lett.* **73**, 332 (1994).

[4] S. Eggert and I. Affleck, *Phys. Rev. Lett.* **75**, 934 (1995).

[5] G. Martins, M. Laukamp, J. Riera, and E. Dagotto, *Phys. Rev. Lett.* **78**, 3563 (1997).

[6] M. Nishino, H. Onishi, K. Yamaguchi, and S. Miyashita, *Phys. Rev. B* **62**, 9463 (2000).

[7] E. Sørensen, I. Affleck, D. Augier, and D. Poilblanc, *Phys. Rev. B* **58**, R14701 (1998).

[8] P. Hansen, D. Augier, J. Riera, and D. Poilblanc, *Phys. Rev. B* **59**, 13557 (1999).

[9] S. Bose, *Phys. Rev. Lett.* **91**, 207901 (2003).

[10] R. Vieira and G. Rigolin, *Physics Letters A* **384**, 126536 (2020).

[11] L. Campos Venuti, C. Degli Esposti Boschi, and M. Roncaglia, *Phys. Rev. Lett.* **96**, 247206 (2006).

[12] L. Campos Venuti, C. Degli Esposti Boschi, and M. Roncaglia, *Phys. Rev. Lett.* **99**, 060401 (2007).

[13] R. Toskovic, R. van den Berg, A. Spinelli, I. S. Eliens, B. van den Toorn, B. Bryant, J.-S. Caux, and A. F. Otte, *Nature Phys* **12**, 656 (2016).

[14] M. Kiczynski, S. K. Gorman, H. Geng, M. B. Donnelly, Y. Chung, Y. He, J. G. Keizer, and M. Y. Simmons, *Nature* **606**, 694 (2022).

[15] K. Karmakar and S. Singh, *Phys. Rev. B* **91**, 224401 (2015).

[16] A. I. Smirnov, V. N. Glazkov, L. I. Leonyuk, A. G. Vekter, and R. M. Eremina, *J. Exp. Theor. Phys.* **87**, 1019 (1998).

[17] S. Bertaina, C.-E. Dutoit, J. Van Tol, M. Dressel, B. Barbara, and A. Stepanov, *Phys. Rev. B* **90**, 060404 (2014).

[18] P. Fournier-Leylekian, P. Auban-Senzier, C. Coulon, O. Jeannin, M. Fourmigué, C. Pasquier, and J.-P. Pouget, *Phys. Rev. B* **84**, 195134 (2011).

[19] J. Zeisner, O. Pilone, L. Soriano, G. Gerbaud, H. Vezin, O. Jeannin, M. Fourmigué, B. Büchner, V. Kataev, and S. Bertaina, *Phys. Rev. B* **100**, 224414 (2019).

[20] L. Soriano, O. Pilone, M. D. Kuz'min, H. Vezin, O. Jeannin, M. Fourmigué, M. Orio, and S. Bertaina, *Phys. Rev. B* **105**, 064434 (2022).

[21] L. Soriano, J. Zeisner, V. Kataev, O. Pilone, M. Fourmigué, O. Jeannin, H. Vezin, M. Orio, and S. Bertaina, *Appl. Magn. Reson.* **51**, 1307 (2020).

[22] K. Uchinokura, *J. Phys. Condens. Matter* **14**, R195 (2002).

[23] H. Ikeuchi, H. De Raedt, S. Bertaina, and S. Miyashita, *Phys. Rev. B* **95**, 024402 (2017).

[24] S. Miyashita and S. Yamamoto, *Phys. Rev. B* **48**, 913 (1993).

[25] X. Fu, L. Huang, K. Liu, J. C. G. Henriques, Y. Gao, X. Han, H. Chen, Y. Wang, C.-A. Palma, Z. Cheng, X. Lin, S. Du, J. Ma, J. Fernández-Rossier, X. Feng, and H.-J. Gao, *Nat. Synth* [10.1038/s44160-025-00743-5](https://doi.org/10.1038/s44160-025-00743-5) (2025).

[26] X. Su, Z. Ding, Y. Hong, N. Ke, K. Yan, C. Li, Y.-F. Jiang, and P. Yu, *Nat. Synth* [10.1038/s44160-025-00744-4](https://doi.org/10.1038/s44160-025-00744-4) (2025).

[27] C. Zhao, G. Catarina, J.-J. Zhang, J. C. G. Henriques, L. Yang, J. Ma, X. Feng, O. Gröning, P. Ruffieux, J. Fernández-Rossier, and R. Fasel, *Nat. Nanotechnol.* **19**, 1789 (2024).

[28] J. P. Pouget, P. Fournier-Leylekian, S. Petit, B. Hennion, C. Coulon, and C. Bourbonnais, *Phys. Rev. B* **96**, 035127 (2017).

[29] J.-P. Pouget, P. Alemany, and E. Canadell, *Mater. Horiz.* **5**, 590 (2018).

[30] M. Fourmigué, E. W. Reinheimer, K. R. Dunbar, P. Auban-Senzier, C. Pasquier, and C. Coulon, *Dalton Trans.* **2008**, 4652 (2008).

[31] L. Soriano, M. Orio, O. Pilone, O. Jeannin, E. Reinheimer, N. Quéméré, P. Auban-Senzier, M. Fourmigué, and S. Bertaina, *J. Mater. Chem. C* , [10.1039/D2TC05431K](https://doi.org/10.1039/D2TC05431K) (2023).

[32] A. Abragam and B. Bleaney, *Electron Paramagnetic Resonance of Transition Ions*, repr ed., The International Series of Monographs on Physics (Oxford Univ. Press, Oxford, 2013).

[33] K. N. Shrivastava, *Phys. Status Solidi B* **117**, 437 (1983).

[34] R. Orbach, *Proc. R. Soc. Lond. A* **264**, 458 (1961).

[35] M. Berberan-Santos, E. Bodunov, and B. Valeur, *Chemical Physics* **315**, 171 (2005).

[36] N. Stein, L. Mainali, J. S. Hyde, and W. K. Subczynski, *Appl Magn Reson* **50**, 903 (2019).

[37] J. C. Phillips, *Rep. Prog. Phys.* **59**, 1133 (1996).

[38] D. C. Johnston, *Phys. Rev. B* **74**, 184430 (2006).

[39] J. H. Van Vleck, *Phys. Rev.* **59**, 724 (1941).

[40] P. L. Scott and C. D. Jeffries, *Phys. Rev.* **127**, 32 (1962).

[41] R. P. Budoyo, K. Kakuyanagi, H. Toida, Y. Matsuzaki, W. J. Munro, H. Yamaguchi, and S. Saito, *Appl. Phys. Express* **11**, 043002 (2018).

[42] W. B. Mims, K. Nassau, and J. D. McGee, *Phys. Rev.* **123**, 2059 (1961).

[43] J. Klauder and P. Anderson, *Phys. Rev.* **125**, 912 (1962).

[44] A. M. Raitsimring and K. M. Salikhov, *Bull. Magn. Reson.* **7**, 34 (1985).

[45] G. Wolfowicz, F. J. Heremans, C. P. Anderson, S. Kanai, H. Seo, A. Gali, G. Galli, and D. D. Awschalom, *Nat Rev Mater* **6**, 906 (2021).

[46] P. Hu and S. R. Hartmann, *Phys. Rev. B* **9**, 1 (1974).

[47] T. Böttger, C. W. Thiel, Y. Sun, and R. L. Cone, *Phys. Rev. B* **73**, [10.1103/physrevb.73.075101](https://doi.org/10.1103/physrevb.73.075101) (2006).

[48] W. B. Mims, *Phys. Rev. B* **5**, 2409 (1972).

[49] M. Chiba and A. Hirai, *J. Phys. Soc. Jpn.* **33**, 730 (1972).

[50] M. Le Dantec, *Electron Spin Dynamics of Erbium Ions in Scheelite Crystals, Probed with Superconducting Resonators at Millikelvin Temperatures*, Ph.D. thesis (2022).

[51] S. Agnello, R. Boscaino, M. Cannas, and F. Gelardi, *Phys. Rev. B* **64**, 174423 (2001).

[52] R. Boscaino and F. Gelardi, *Phys. Rev. B* **46**, 14550 (1992).

[53] M. Rančić, M. Le Dantec, S. Lin, S. Bertaina, T. Chanelière, D. Serrano, P. Goldner, R. B. Liu, E. Flurin, D. Estève, D. Vion, and P. Bertet, *Phys. Rev. B* **106**, 144412 (2022).

[54] H.-J. Lim, S. Welinski, A. Ferrier, P. Goldner, and J. J. L. Morton, *Phys. Rev. B* **97**, 064409 (2018).

[55] J. H. Shim, S. Bertaina, S. Gambarelli, T. Mitra, A. Müller, E. I. Baibekov, B. Z. Malkin, B. Tsukerblat, and B. Barbara, *Phys. Rev. Lett.* **109**, 050401 (2012).

[56] D. Kaminski, A. L. Webber, C. J. Wedge, J. Liu, G. A. Timco, I. J. Vitorica-Yrezabal, E. J. L. McInnes, R. E. P. Winpenny, and A. Ardavan, *Phys. Rev. B* **90**, 184419 (2014).

[57] P. Anderson and P. Weiss, *Rev. Mod. Phys.* **25**, 269 (1953).

[58] S. R. White, *Phys. Rev. Lett.* **69**, 2863 (1992).

[59] J. Hauschild and F. Pollmann, *SciPost Phys. Lect. Notes* , 5 (2018).

[60] J. Pescia, *La Relaxation Des Spins Électroniques Avec Le Réseau (Théorie Élémentaire et Méthodes de Mesure Du Temps T1)*, Vol. 27 (1966).

[61] C. B. P. Finn, R. Orbach, and W. P. Wolf, *Proc. Phys. Soc.* **77**, 261 (1961).

[62] L. Gu and R. Wu, *Phys. Rev. B* **103**, 014401 (2021).

[63] B. Faughnan and M. Strandberg, *Journal of Physics and Chemistry of Solids* **19**, 155 (1961).

[64] R. Kubo and K. Tomita, *J. Phys. Soc. Jpn.* **9**, 888 (1954).

Supplementary Information

Exploring electron spin dynamics in spin chains using defects as a quantum probe.

S1. DMRG CALCULATIONS

The simulations of the quantum systems were carried out using tensor networks and the Density Matrix Renormalisation Group (DMRG) method [58]. The tensor network calculations were performed using the Python library TENPY [59]. It is important to note that DMRG is an approximation of the true ground state. There can be potential issues with convergence and small numerical errors, DMRG has shown is robustness for 1D non frustrated system. The SVD cut-off was set to 10^{-10} , while the convergence criterion for the ground energy was a relative change of 10^{-10} . We have calculated the ground state and sometimes the 1st excited state. Thanks to TENPY, the scripts run smoothly from some seconds to some minutes on the heavier calculation on an Apple macbook pro 2021 M1Max with 64Go of RAM.

While changing the value of δ we have computed the distribution of magnetization for an odd number of spin chain (see Fig. S1). It is worth to notice that for $\delta = \pm 1$ which correspond to uncoupled dimer, the local magnetisation is zero excepted at the site immediately after the defect. When decreasing $\|\delta\|$ the polarization spreads until $\delta = 0$ (*i.e.* the uniform spin chain) where the magnetization is now through the entire chain.

In order to estimate the effect of the dimerization factor δ on the dipol-dipol interaction between two edge state, we have calculated the triplet gap between two 51 spins chains connected to an Ising interaction of value d . In the non interacting case: $\delta = 1$ the coupling is only between the 2 isolated spin at the end. We can see that the dipol-dipol remains unchanged ($d_{eff} = d$). on the contrary in the case of uniform spin chain ($\delta=0$) the effective dipolar file tend to be extremely reduced ($d_{eff} \sim 0$). In the case of (*o*-DMTTF)₂*X*, δ is close to 0.1 and $d_{eff} \sim 0.3$

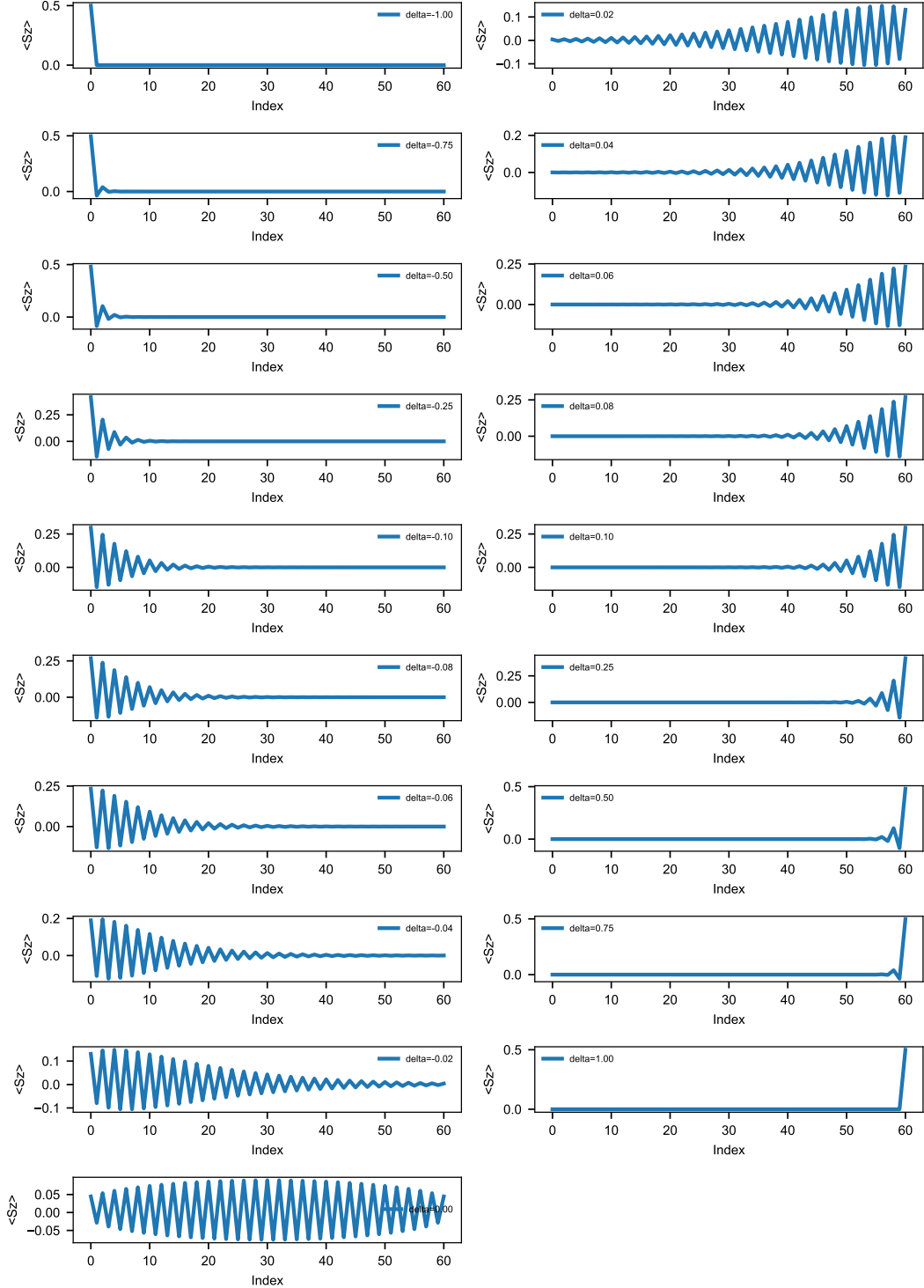


Figure S1. partial Magnetization Profiles for Open Spin Chains with Varying Dimerization. Local magnetization ($\langle S_z \rangle$) profiles, obtained through Density Matrix Renormalization Group (DMRG) calculations, are shown for open spin chains of $L=60$ sites. The dimerization parameter, δ , is varied across a range spanning from -1.00 to +1.00, including $\delta=0$ to represent the uniform spin chain. For each value of δ , the spin polarization arising from the open boundary conditions is clearly visible. These profiles illustrate the complex evolution of spin localization and correlation effects as the dimerization strength is modulated, transitioning from a regime of strong spin localization at the ends for large $|\delta|$ to a more homogeneous spin distribution for small $|\delta|$. Note that the edge polarization diminishes in magnitude as $|\delta|$ approaches zero.

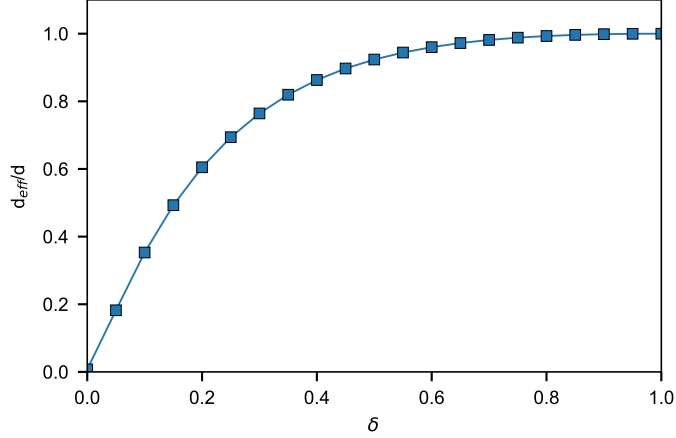


Figure S2. Effective dipole-dipole field as function of the dimerization factor δ

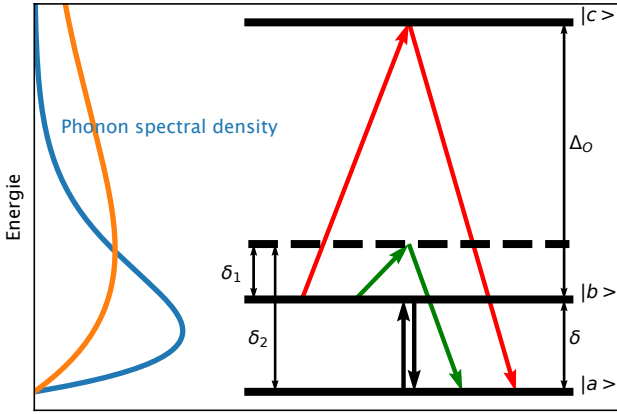


Figure S3. Diagram illustrating the three subsystems involved in lattice relaxation.

S2. SPIN-PHONON INTERACTIONS

To understand the processes involved in spin relaxation process, it is essential to distinguish three subsystems: the spins, the lattice, and a thermal reservoir referred to as the bath [60]. The spins interact with lattice phonons via spin-orbit coupling; the lattice vibrates. The lattice and the bath exchange heat through thermal contact. The lattice has a low heat capacity, while the bath, by definition, has an infinite capacity. If the thermal contact between the bath and the lattice is efficient, they remain in thermal equilibrium $T_p = T_0$. This assumption is valid for describing the direct, Orbach, and Raman processes.

When the bath and the lattice exchange heat poorly, phonon-bath relaxation becomes non-negligible compared to spin-phonon relaxation. The lattice phonons, being few in number, heat up to a temperature $T_p \neq T_0$ and slow down spin-lattice relaxation. This phenomenon is called the "phonon bottleneck" [40].

S2.1. Direct Process

Consider a two-level magnetic system $\{|a\rangle, |b\rangle\}$ separated by the Zeeman energy $E_z = g\mu_B H_0$. The direct relaxation process results from the absorption and emission of a lattice phonon with energy $\delta = \hbar\omega = g\mu_B H_0$. Here, it is assumed that the lattice and bath are in continuous equilibrium. The spin populations n_a and n_b of each level evolve according to equation (S1), where $w_{a \rightarrow b}$ is the transition probability from state $|a\rangle$ to state $|b\rangle$ per unit time, and vice versa for $w_{b \rightarrow a}$.

$$\frac{dn_b}{dt} = -\frac{dn_a}{dt} = w_{a \rightarrow b} n_a - w_{b \rightarrow a} n_b \quad (\text{S1})$$

The spectral density of the phonon population $\rho(\omega)$ is given by equation (S2), where $g_D(\omega)$ represents the Debye density of states in three-dimensional space, and v is the speed of sound in the medium [32]. K is a temperature-independent coefficient.

$$\rho(\omega)d\omega = g_D(\omega)\bar{p}_0(\omega)d\omega \quad (\text{S2})$$

$$g_D(\omega) = \frac{3\omega^2}{2\pi^2 v^3} ; \bar{p}_0(\omega) = \frac{1}{e^{\hbar\omega/k_B T_0} - 1} \quad (\text{S3})$$

$$w_{b \rightarrow a} = K[1 + \bar{p}_0(\omega)] ; w_{a \rightarrow b} = K\bar{p}_0(\omega) \quad (\text{S4})$$

Introducing $n = n_- - n_+$ as the difference between the spin populations and $N = n_- + n_+$ as the total spin population, and combining equations (S1) and (S4), we derive:

$$\frac{dn}{dt} = 2K[-n_+\bar{p}_0(\omega) - n_+ + n_-\bar{p}_0(\omega)] \quad (\text{S5})$$

$$\frac{dn}{dt} = K[(1 + 2\bar{p}_0(\omega))n - N] \quad (\text{S6})$$

In equation (S5), we can identify, in sequence, stimulated emission, spontaneous emission, and the absorption of a phonon with energy $\hbar\omega$. At equilibrium, $T_s = T_0$ and $n = n_0 = N \tanh\left(\frac{\hbar\omega}{2k_B T_0}\right)$ is the thermal equilibrium polarization.

$$\frac{dn}{dt} = -\frac{1}{T_{1d}}(n - n_0) \quad (\text{S7})$$

From this, the temperature dependence of T_1 in the case of the direct process is deduced (S8). The coefficient K can be determined from $g(\omega)$ and by calculating the transition probability using perturbation theory [40]. For a Kramers doublet, the relation (S8) is found:

$$\frac{1}{T_{1d}} = \alpha_D g^3 B^5 \coth\left(\frac{\hbar\omega}{2k_B T}\right) \quad (\text{S8})$$

since our base temperature is 5.5K, $\hbar\omega \ll 2k_B T$ and we can approximate $\coth\left(\frac{\hbar\omega}{2k_B T}\right) \approx \frac{2k_B T}{\hbar\omega}$ and so at the resonance

$$\frac{1}{T_{1d}} = \alpha'_D B_0^4 T \quad (\text{S9})$$

for a Kramers doublet.

S2.2. Resonant Two-Phonon Process: Orbach

In the Orbach-type process, we consider a third energy level $|c\rangle$ separated by Δ_O from the level $|b\rangle$ and by $\Delta_O + \delta$ from the fundamental level $|a\rangle$. This process can only exist under the condition $\Delta_O < k_B\theta_D$, where θ_D is the Debye temperature [34, 61]. The transition from state $|b\rangle$ to $|a\rangle$ occurs in two steps: absorption of a resonant phonon with energy Δ_O and emission of a resonant phonon with energy $\Delta_O + \delta$, as shown in figure S2.

$$w_{b \rightarrow c} = B[1 + \bar{p}_0(\Delta_0)] ; w_{c \rightarrow b} = B\bar{p}_0(\Delta_0) \quad (\text{S10})$$

$$w_{a \rightarrow c} = B[1 + \bar{p}_0(\Delta_0 + \delta)] ; w_{c \rightarrow a} = B\bar{p}_0(\Delta_0 + \delta) \quad (\text{S11})$$

$$\begin{cases} \frac{dn_a}{dt} = B[n_c(\bar{p}_0(\Delta_0 + \delta) + 1) - n_a\bar{p}_0(\Delta_0 + \delta)] \\ \frac{dn_b}{dt} = B[n_c(\bar{p}_0(\Delta_0) + 1) - n_b\bar{p}_0(\Delta_0)] \end{cases} \quad (\text{S12})$$

In many cases, the spin population of the third energy level can be considered small compared to the other two, $n_c \ll n_b, n_a$, and $\delta \ll \Delta_0$. The system of equations (S12) simplifies, and similarly to the direct process subsection S2S2.1, we find:

$$\frac{dn}{dt} = -1/T_{1O}(n - n_0) \quad (\text{S13})$$

It can be shown that for a Kramers doublet, T_{1O} follows the relation (S14):

$$1/T_{1O} = \alpha_o \Delta_0^3 e^{-\Delta_0/T} \quad (\text{S14})$$

S2.3. Non-Resonant Two-Phonon Process: Raman

The Raman process corresponds to the simultaneous absorption of a phonon with energy δ_1 and the emission of a phonon with energy $\delta_2 = \delta_1 + \delta$ to achieve a spin flip from $|b\rangle$ to $|a\rangle$. Unlike the Orbach process, the phonons are not constrained by the value of the gap Δ_O , and if $\delta \ll k_B\theta_D$, then the entire phonon energy spectrum is accessible up to θ_D . The only condition to satisfy is $\delta_2 - \delta_1 = \delta$. To calculate the transition probabilities per unit time $w_{b \rightarrow a}$ and $w_{a \rightarrow b}$, we consider $H_c^{(2)}$, the second-order perturbation of the spin-phonon coupling Hamiltonian. We then sum over all possible energies of δ_1 :

$$w_{b \rightarrow a} = \int \frac{2\pi}{\hbar} |\langle b, \underline{\bar{p}_0(\delta_1)}, \bar{p}_0(\delta_2) | H_c^{(2)} | a, \bar{p}_0(\delta_1) + 1, \underline{\bar{p}_0(\delta_2) + 1} \rangle|^2 \rho(\delta_2) \rho(\delta_1) d\delta_1 \quad (\text{S15})$$

$$w_{a \rightarrow b} = \int \frac{2\pi}{\hbar} |\langle a, \underline{\bar{p}_0(\delta_1) + 1}, \bar{p}_0(\delta_2) + 1 | H_c^{(2)} | b, \bar{p}_0(\delta_1), \underline{\bar{p}_0(\delta_2)} \rangle|^2 \rho(\delta_2) \rho(\delta_1) d\delta_1 \quad (\text{S16})$$

$$\frac{dn_b}{dt} = -\frac{dn_a}{dt} = K' \int n_a \bar{p}_0(\delta_2)(1 + \bar{p}_0(\delta_1)) - n_b \bar{p}_0(\delta_1)(1 + \bar{p}_0(\delta_2)) \delta_1^6 d\delta_1 \quad (\text{S17})$$

Similarly to the direct process section S2S2.1, we find the equilibrium return equation (S18):

$$\frac{dn}{dt} = -\frac{1}{T_{1R}}(n - n_0) \quad (\text{S18})$$

$$\frac{1}{T_{1R}} = K'' \int_0^{\theta_D} \frac{\delta_1^6 e^{\delta_1/k_B T}}{(e^{\delta_1/k_B T} - 1)^2} \quad (\text{S19})$$

The integral (S19) can be simplified if we assume that the temperature T is low compared to the Debye temperature θ_D . This assumption is generally valid when measuring T_1 at temperatures close to liquid helium. In the case where the system is a Kramers doublet, we find the relation (S20):

$$1/T_{1R} = \alpha_R T^9 \quad (\text{S20})$$

The Raman process always exists, but the dependence of T_{1R} on temperature or magnetic field is strongly modified depending on the value of θ_D , the nature, or the size of the system [62].

S2.4. Phonon Bottleneck Effect

The phonon bottleneck effect manifests when the thermal contact between the lattice and the bath is poor. The lattice phonons are no longer necessarily in equilibrium with the bath at temperature T_0 [40]. We now consider $\bar{p}(\omega)$ as the phonon population of the lattice at temperature T_p .

$$\bar{p}(\omega) = \frac{1}{e^{\hbar\omega/k_B T_p} - 1} \quad (\text{S21})$$

$$\frac{dn}{dt} = 2\rho(\omega)[n_b w_{b \rightarrow a}(\bar{p} + 1) - n_a w_{b \rightarrow a}\bar{p}] \quad (\text{S22})$$

$$\begin{cases} \frac{dn}{dt} = -\frac{1}{T_{1d}}[n - n_0 - n \frac{\bar{p} - \bar{p}_0}{\bar{p}_0 + 1/2}] \\ \frac{d\bar{p}}{dt} = -\frac{1}{\rho(\delta)\Delta\delta} \frac{dn}{dt} - \frac{\bar{p} - \bar{p}_0}{T_{ph}} \end{cases} \quad (\text{S23})$$

Faughnan and Strandbergh numerically calculated the solutions (S23) [63] and showed that $n(t)$ and $\bar{p}(t)$ are not monoexponential. They present a short relaxation time T'_{1b} and a long relaxation time T_{1b} , both of which can be expressed in terms of the bottleneck parameter σ .

$$T_{1b} = (1 + \sigma)T_{1d} \quad (\text{S24})$$

$$T'_{1b} = \frac{T_{ph}}{\sigma} \quad (\text{S25})$$

The bottleneck factor σ is very important. It is the ratio of the energy exchanged between the spins and the phonons relative to the energy exchanged between the phonons and the bath.

$$\sigma = \frac{E_z T_{ph}}{E_{ph} T_{SP}} = \frac{T_{ph} n_0}{T_{1d} \rho(\delta) \Delta\delta \coth(\frac{\delta}{2k_B T})} \quad (\text{S26})$$

When $\sigma \ll 1$, the bottleneck effect is not visible, so $T_{1b} = T_{1d}$, and the direct process correctly describes the spin relaxation. Conversely, when $\sigma \gg 1$, we speak of a severe bottleneck effect, and the measured relaxation time is significantly extended, $T_{1b} \simeq \sigma T_{1d}$. The relation (S27) is valid if $\delta \ll k_B T$:

$$T_{1b} \simeq \sigma T_{1d} = D \coth(\frac{\delta}{2k_B T})^2 \simeq D' T^2 \quad (\text{S27})$$

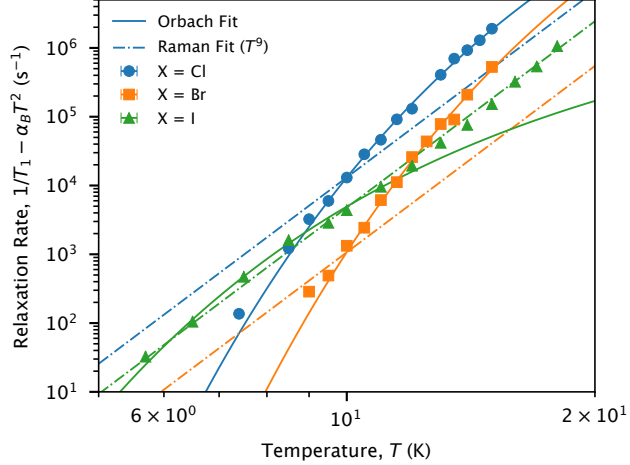


Figure S4. Spin lattice relaxation rate corrected by the phonon-bottleneck process presented in log-log scale. For the three compounds we have fitted using the two possible model : Orbach (plain line) and Raman (dashed dot line) processes

$$D' = \frac{6\Delta\delta k_B^2}{\pi^2 n v^3 \hbar^3 T_{ph}} \quad (\text{S28})$$

Faughnan and Strandbergh propose a simplified equation for $n(t)$ in the case $T_{1d} \gg T_{ph}$ (S29) [63]. This condition is generally satisfied. The equation (S29) has no trivial solution except for $\sigma = 0$, where $n(t)$ is an exponential law.

$$-\frac{t}{T_{1d}} = (1 + \sigma) \ln \left(\frac{n_0}{n - n_0} \right) - \sigma \frac{n}{n_0} \quad (\text{S29})$$

The solution $n(t)$ can be numerically calculated from equation (S29).

S2.5. Statistical Goodness of fit model

In The main text, we present spin lattice relaxation of $(o\text{-DMTTF})_2\text{Br}$, $(o\text{-DMTTF})_2\text{Cl}$ and $(o\text{-DMTTF})_2\text{I}$ using the chosen model (Orbach or Raman). Here we show the fit for both model confronted to every samples including error and R^2 estimation.

Table S1. Fitted parameters of spin lattice relaxation.

Model	$\alpha_{R9} \times 10^{-6} (\text{s}^{-1} \text{K}^{-9})$	$\alpha_O \times 10^4 (\text{s}^{-1} \text{K}^{-3})$	$\Delta_O (\text{K})$	R^2
$(o\text{-DMTTF})_2\text{Cl}$	Raman	13.1 ± 3.3	-	-
	Orbach	-	1.13 ± 0.3	147 ± 4
$(o\text{-DMTTF})_2\text{Br}$	Raman	1.1 ± 0.8	-	-
	Orbach	-	1.6 ± 0.4	181 ± 17
$(o\text{-DMTTF})_2\text{I}$	Raman	4.17 ± 0.17	-	-
	Orbach	-	0.0015 ± 0.0001	70 ± 2

The value of R^2 clearly prove that Orbach process is involved in the relaxation of $(o\text{-DMTTF})_2\text{Cl}$ and $(o\text{-DMTTF})_2\text{Br}$ while Raman process dominates in $(o\text{-DMTTF})_2\text{I}$.

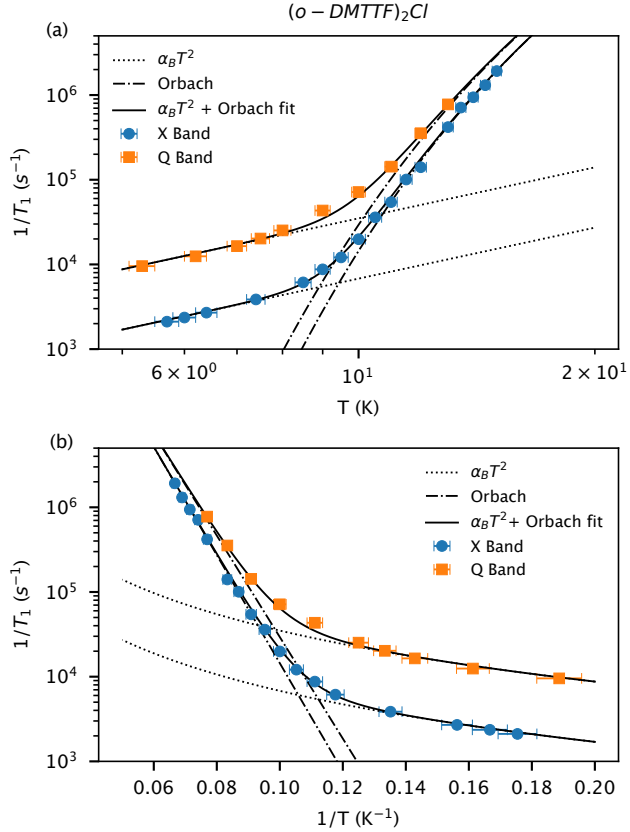


Figure S5. Temperature dependence of the inverse stretched relaxation time ($1/T_1^{\text{str}}$) for $(o\text{-DMTTF})_2\text{Cl}$, plotted against temperature (a) or the inverse of temperature (b) in a log-log scale, and measured at two microwave frequencies: X-band (9.7 GHz) and Q-band (34 GHz). The data are obtained via inversion recovery experiments at variable temperatures between 6 K and 20 K. The dashed lines represent the high temperature Orbach process and the dot line the phonon-bottleneck direct process. The plain black line is the sum of the two contribution

S2.6. Spin lattice relaxation of $(o\text{-DMTTF})_2\text{Cl}$ and $(o\text{-DMTTF})_2\text{I}$

The main text presents the spin lattice relaxation data of $(o\text{-DMTTF})_2\text{Br}$. Here we show the remaining systems.

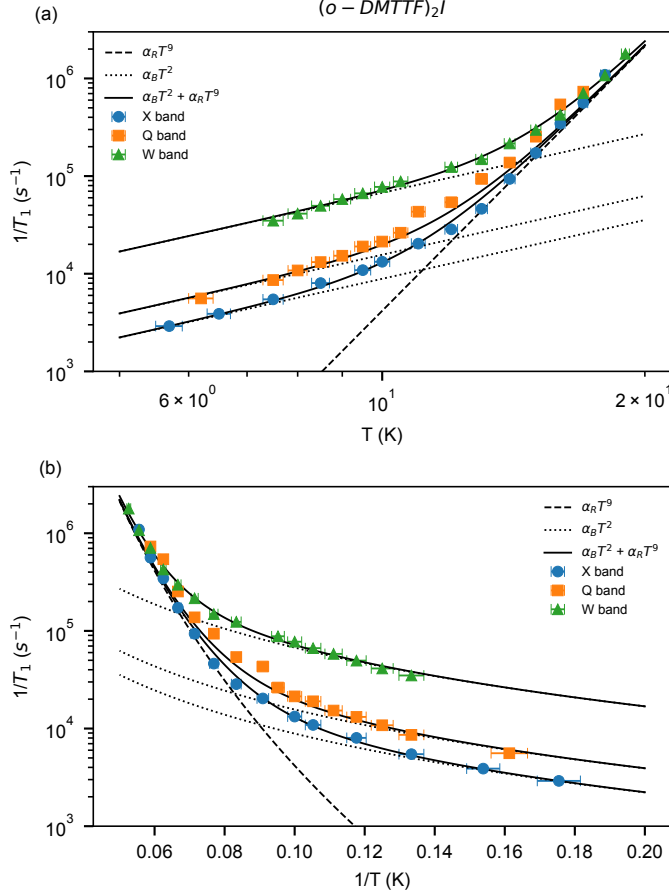


Figure S6. Temperature dependence of the inverse stretched relaxation time ($1/T_1^{\text{str}}$) for $(o\text{-DMTTF})_2\text{I}$, plotted against temperature (a) or the inverse of temperature (b) in a log-log scale, and measured at three microwave frequencies: X-band (9.7 GHz), Q-band (34 GHz), and W-band (94 GHz). The data are obtained via inversion recovery experiments at variable temperatures between 6 K and 20 K. The dashed lines represent the high temperature Raman process and the dot line the phonon-bottleneck direct process. The plain black line is the sum of the two contribution

S3. INSTANTANEOUS DIFFUSION

The main text introduces instantaneous diffusion as a significant decoherence mechanism affecting the Hahn echo decay. It outlines the theoretical basis where the coherence time T_2 is shown to depend on the refocusing pulse angle (θ_2) due to ID. While the main text features a detailed analysis of ID for $(o\text{-DMTTF})_2\text{I}$ (Fig. 6), this section provides the equivalent experimental two-pulse echo (2PE) decay measurements and the fitting according to Eq. (12) for the $(o\text{-DMTTF})_2\text{Cl}$ and $(o\text{-DMTTF})_2\text{Br}$ systems (shown in Figures S7 to S10). Figures S7, S8 and S9 display the raw 2PE decays for various refocusing pulse durations (t_p , which is proportional to θ_2), from which individual T_2 values are extracted. Figure S10 then shows the plots of $1/T_2$ versus the refocusing pulse parameters for chloride and bromide, analogous to Figure 6 for the iodide compound. In our experiment $\pi/2 = 24$ ns and θ_2 was set by changing the pulse time from 8ns every 2ns

Concentration calculation procedure

In the main text we compare two concentration values for each compounds. One obtained from a previous work [20] by continuous wave EPR (C_{cw}) and one obtained from instantaneous diffusion C_{ID} (present work). Here were details the procedures: We start with the concentration in "defects per formula unit" from [20], which was determined by fitting the intensity of the EPR line and is directly related to the static susceptibility. We convert this dimensionless value to a volumetric concentration (in cm^{-3}) using the molar mass of the $(o\text{-DMTTF})_2X$ compound and its crystallographic density, which is known accurately from X-ray diffraction data ([18]). The formula used is: $(C_{\text{cw}} = (\text{defects}/\text{formula unit}) \times M \times \rho)$

unit) $\times (\rho \times N_A)/M$, where ρ is the density, N_A is Avogadro's number, and M is the molar mass. The main source of error comes from the fit of the EPR susceptibility data, which we estimated to be around 10% is due to the error in quantitative EPR. This estimation of error is classic in the quantitative EPR of isotropic $S=1/2$ spins.

Regarding C_{ID} obtained by instantaneous diffusion, the method is completely different. We measured the echo decay by increasing the refoculisation pulse length, then we fitted the decay time and the standard deviation error which is usually within 1% error. We then plot the inverse of the decay time as function of $\langle \sin^2 \theta \rangle$ and we have fitted the slope with an error of about 4%.

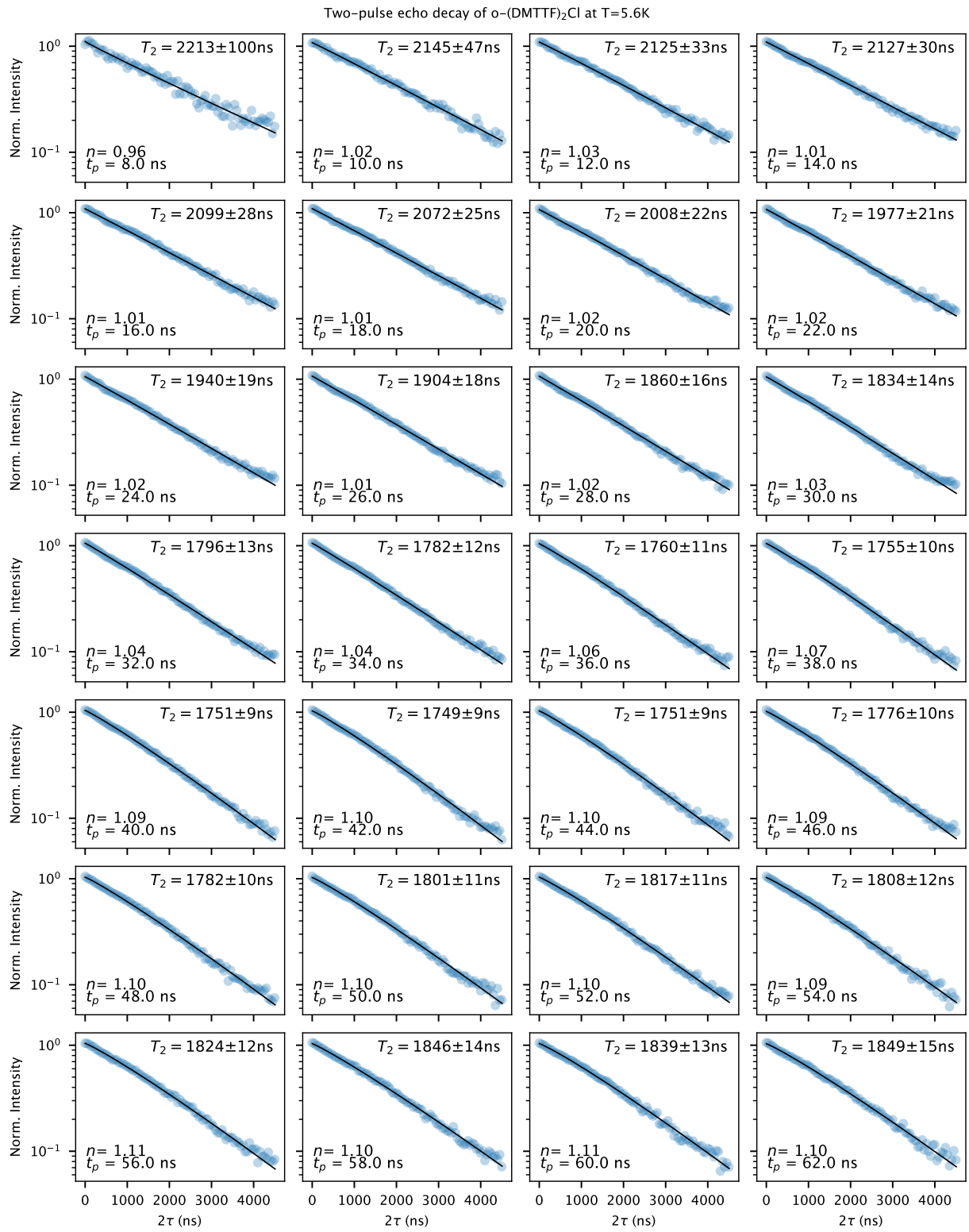


Figure S7. Two-pulse echo decay measurements for $(o\text{-DMTTF})_2\text{Cl}$ at $T = 5.6\text{K}$. The series of plots shows the decay of the spin echo signal as a function of the delay time τ between the excitation pulse ($\pi/2$) and the refocusing pulse (θ_2) induced by different durations (tp) of the second pulse. These pulse durations are indicated in each graph, showing a change of decoherence rate for different duration pulse. Each solid blue lines corresponds to single exponential fits, resulting in the determination of T2 values displayed at the top of each panel

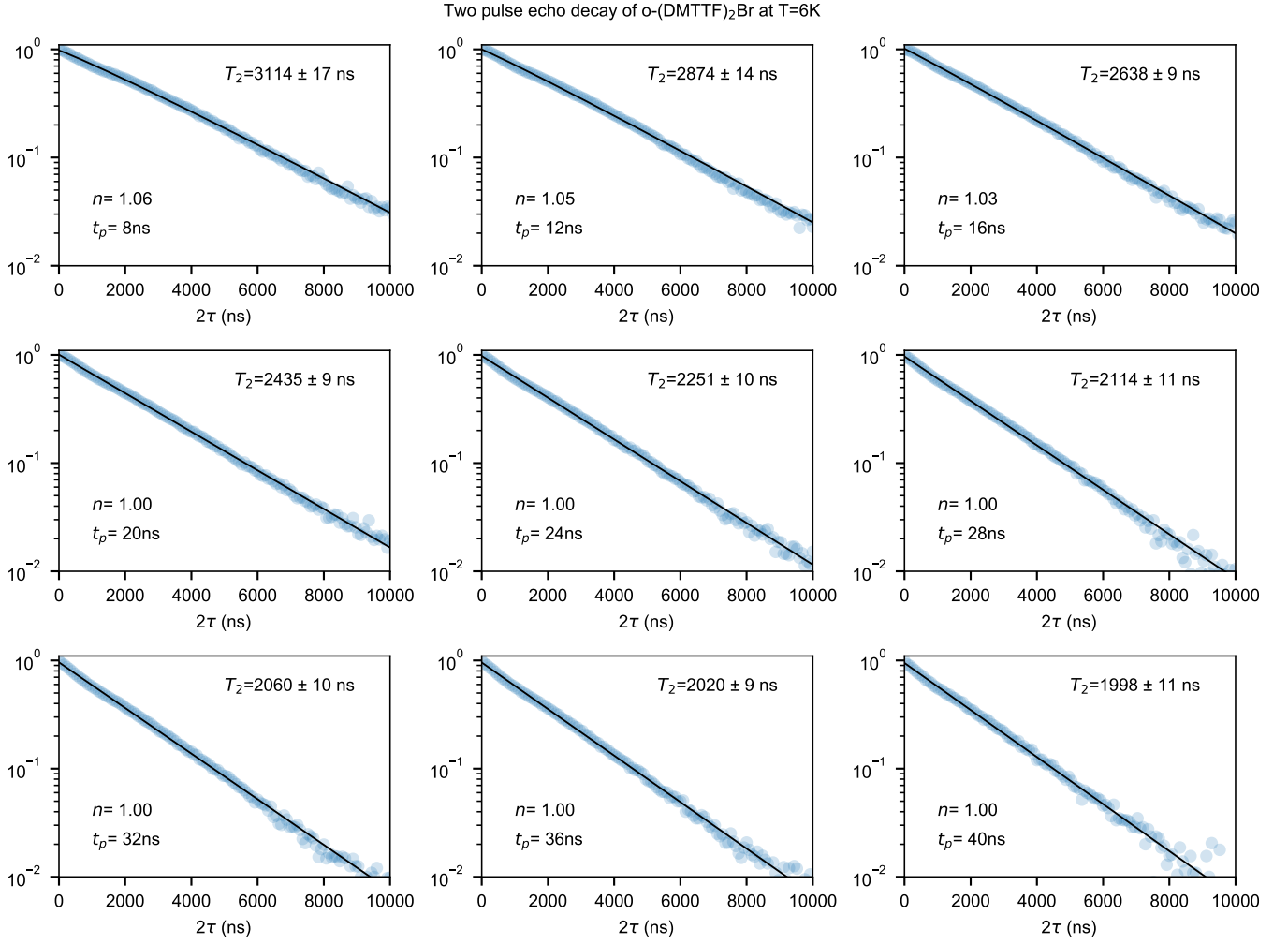


Figure S8. Two-pulse echo decay measurements for (o-DMTTF)₂Br at T = 6K. The series of plots shows the decay of the spin echo signal as a function of the delay time τ between the excitation pulse ($\pi/2$) and the refocusing pulse (θ_2) induced by different durations (t_p) of the second pulse. These pulse durations are indicated in each graph, showing a change of decoherence rate for different duration pulse. Each solid blue lines corresponds to single exponential fits, resulting in the determination of T_2 values displayed at the top of each panel

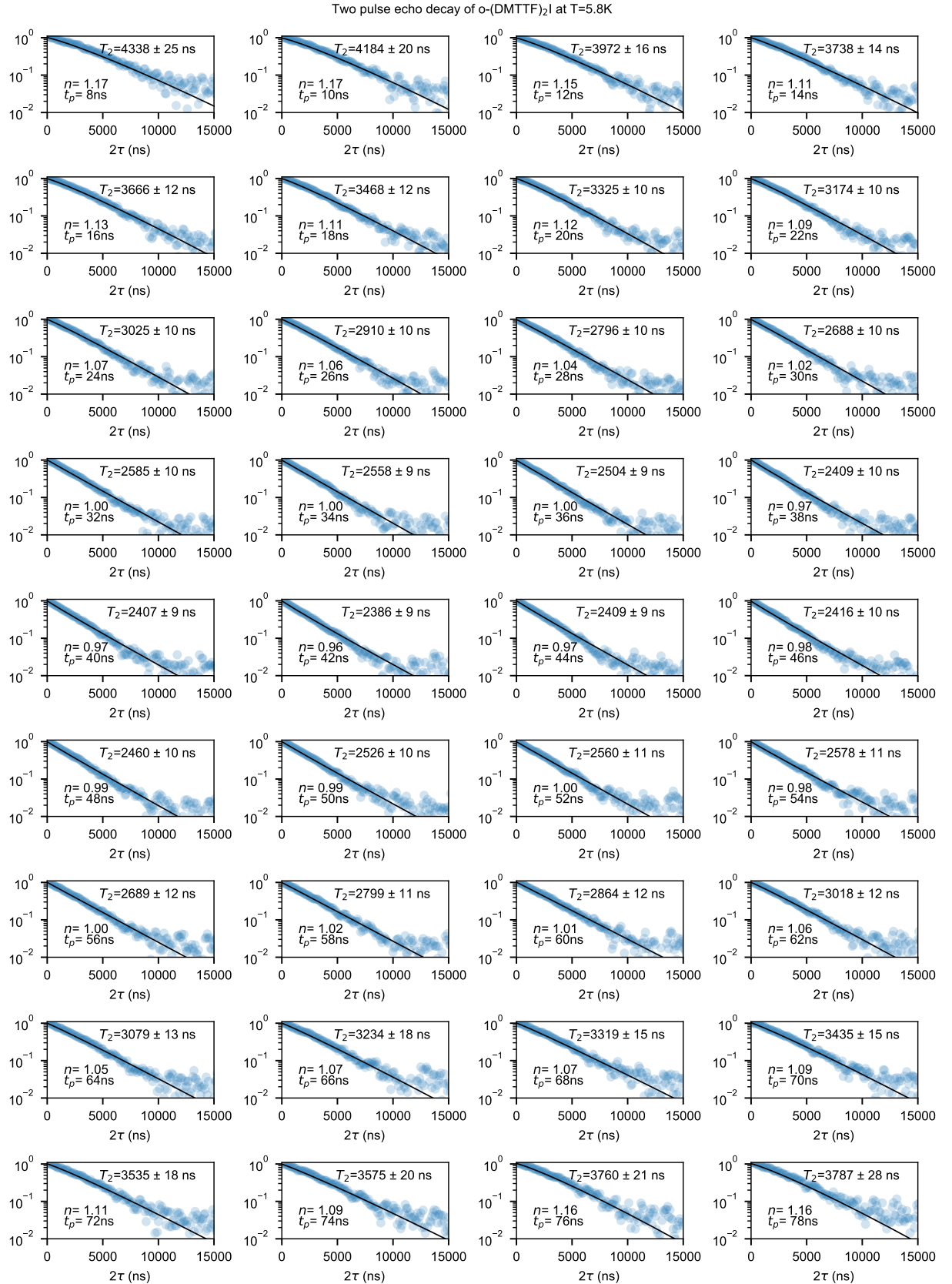


Figure S9. Two-Pulse Echo Decay Measurements for $(o\text{-DMTTF})_2\text{I}$ at 5.8 K with Varying Pulse Durations. A series of two-pulse Hahn echo decay curves are presented for $(o\text{-DMTTF})_2\text{I}$, measured at a temperature of 5.8 K. Each panel shows the decay of the spin echo signal amplitude as a function of the delay time (2τ) between the excitation pulse ($\pi/2$) and the refocusing pulse θ_2 . The duration of the refocusing pulse (denoted as t_p), is systematically varied for each decay series. The solid lines represent the best fits to the experimental data using a stretched exponential decay function, from which the coherence time (T_2) and the stretched parameter n is extracted.

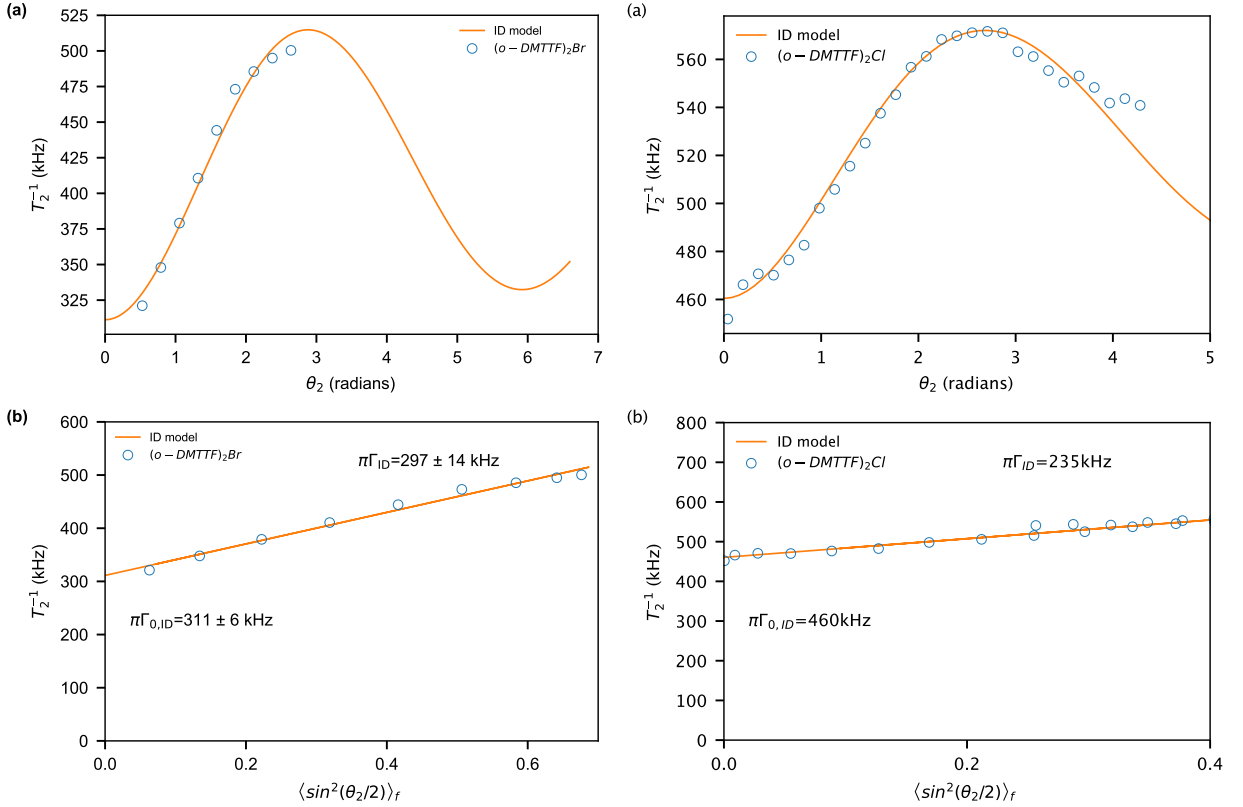


Figure S10. Two-Pulse Echo Decay Measurements for $(o\text{-DMTTF})_2\text{Br}$, and $(o\text{-DMTTF})_2\text{Cl}$ Compounds. This figure presents a series of two-pulse echo decay curves using the same protocol than Fig. 6. Each plot illustrates the decay of the spin echo signal amplitude as a function of the delay time (2τ) between the excitation pulse ($\pi/2$) and the refocusing pulse (θ_2). The refocusing pulse duration (t_p) is systematically varied to observe changes in the decoherence rate. Solid lines represent the best fits to the experimental data using (11)

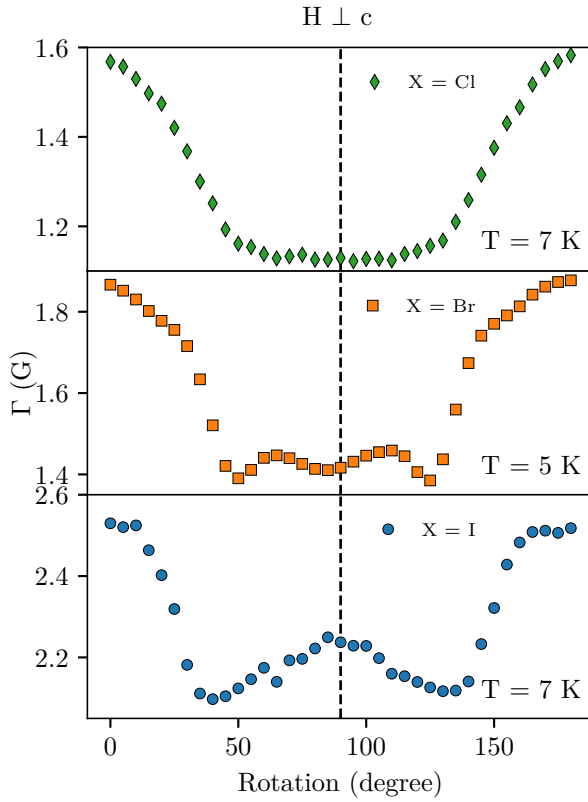


Figure S11. Angular dependence of the half width at half maximum with respect of the external maagnetic field. The purpose of this fugure is to provide the linewidth used for the ID calculation.

S4. SPIN-FLIP RATE

The spectral diffusion analysis reveals the crucial role of the spin-flip rate, denoted by R , in governing electron spin decoherence. This rate quantifies the frequency with which a spin in the surrounding environment, either electronic or nuclear, undergoes a transition that affects the local magnetic field experienced by the central, probed spin. The spin-flip rate, R , of group B spins acts as a key parameter within our theoretical model, describing the influence of the surrounding spin environment on the probed electron spin. Physically, this rate reflects the frequency at which spins in the environment undergo transitions, such as spin-lattice relaxation or flip-flops, thereby changing the local magnetic field and contributing to decoherence of the central spin. Our analysis of the spin-flip rate assumes, for simplicity, an isotropic g-factor. In this case, the spin flip rate can be decomposed into contributions from two distinct processes: spin-lattice relaxation (with rate $1/T_1$) and flip-flops (with rate R_{ff}). The spin-lattice relaxation process is mediated by phonons and is characterized by the interaction of the spin with the lattice vibrations, and is described by the Fermi Golden Rule. The flip-flop process, on the other hand, involves the mutual exchange of spin states between two or more interacting spins.

1. Spin-lattice flip rate

As explained in Section III, relaxation is dominated by the direct phonon bottleneck process in our temperature range. If the perturbing spins are Kramers ions, their T_1 spin flip rate is

$$\frac{1}{T_1^{\text{phb}}} = \frac{3\omega^2\Delta\omega}{2\pi^2v^3n\tau_{\text{ph}}} \coth^2\left(\frac{\hbar\omega}{2k_B T}\right) \quad (\text{S30})$$

where v the velocity of sound in the crystal, $\Delta\omega$ is the resonance linewidth, n is the concentration of spins, and τ_{ph} is the latticeâŠbath relaxation time. Assuming $k_B T \gg \hbar\omega$, and the inhomogenous linewidth is field dependent we can simplify by

$$\frac{1}{T_1^{\text{phb}}} = \alpha'_B H_0 T^2 \quad (\text{S31})$$

2. Flip-flop rate

The flip-flop rate can be estimated following the analysis done in [47]:

$$R_{\text{ff}} \approx \frac{2\pi}{\hbar} \left(|\langle \uparrow\downarrow | H_{dd, \text{spin } i - \text{spin } j} | \downarrow\uparrow \rangle|^2 \right)_{\text{avg}} \frac{1}{\hbar\Gamma_{inh}} = \left(\frac{\pi\mu_0\mu_B g^2 C}{9\sqrt{3}\hbar} \right)^2 \cdot \frac{1}{\Gamma_{inh}} \quad (\text{S32})$$

Using the concentration of QSD-EC and the linewidth of figure S11 we obtain :

$R_{\text{ff}} = 16.5$ kHz, 24.3 kHz and 14 kHz for $(o\text{-DMTTF})_2\text{Cl}$, $(o\text{-DMTTF})_2\text{Br}$ and $(o\text{-DMTTF})_2\text{I}$ respectively.

S5. ESTIMATION OF INTERNAL PROCESS IN THE DECOHERENCE

S5.1. Method of moments

In the case of pure random process, Anderson and Weiss [57] and Kubo et Tomita [64] have estimated that the sources of broadening which are included in the second moment of the distribution is reduced by the exchange interaction J .

The method of moments is a statistical technique used to analyze the shape and characteristics of spectral lines, particularly when the line shape is described by a Gaussian function. A Gaussian function is given by:

$$f(x) = \frac{1}{\sigma\sqrt{2\pi}} e^{-\frac{(x-\mu)^2}{2\sigma^2}}$$

where μ is the mean and σ is the standard deviation.

For a distribution f , the n -th moment about the mean is defined as:

$$M_n = \int_{-\infty}^{\infty} (x - \mu)^n f(x) dx$$

The second moment about the mean, measures the spread or width of the Gaussian spectral line:

$$M_2 = \int_{-\infty}^{\infty} (x - \mu)^2 f(x) dx = \sigma^2 \quad (\text{S33})$$

Considering the half width at half maximum of the distribution Γ_d , we obtain $M_2 = \Gamma^2 / 2 \ln 2$.

For electron electron interaction we obtain : $M_2^{e-e} = \left(\mu_0 \mu_B^2 g^2 C_{tot} / (9\sqrt{3}\hbar) \right)^2 / 2 \ln 2 \simeq 3 \times 10^{17} \text{Hz}^2$ where C_{tot} is the total concentration of spins

For anisotropic exchange interaction we used $M_2^{ani} = ((\Delta g/g)^2 J)^2$, using $\Delta g/g = 0.004$ and $J \sim 600 \text{ K}$ [20] we obtain $M_2^{ani} = 4 \times 10^{16} \text{Hz}^2$

S6. STRETCHED EXPONENTIAL

The stretched exponential function arises in systems where relaxation dynamics are influenced by a distribution of rates instead of a single relaxation process. Following Johnston article [38] let's summarize the main results. Experimentally we can fit the spin lattice relaxation using :

$$\langle S_z \rangle = \langle S_z \rangle_0 \exp \left[- \left(\frac{t}{T_1^{\text{str}}} \right)^\beta \right] \quad (\text{S34})$$

in the case of $0 < \beta < 1$ eq. (S34) becomes

$$\exp \left[- \left(\frac{t}{T_1^{\text{str}}} \right)^\beta \right] = \int_0^{\infty} P(s, \beta) e^{-s \frac{t}{T_1^{\text{str}}}} ds \quad (\text{S35})$$

where $s = \frac{T_1^{\text{str}}}{T_1}$ and $P(s, \beta)$ the probability density of s knowing β . In the particular case of $\beta = 1$, the relaxation is a monoexponential decay, $P(s, \beta = 1)$ is a Dirac function $\delta(s = 1)$ and $T_1^{\text{str}} = T_1$. For a general β , eq. (S35) is Laplace transform of $P(s, \beta)$ and consequently, $P(s, \beta)$ can be obtained by the inverse Laplace transform of the stretched exponential:

$$P(s, \beta) = \frac{1}{2\pi i} \int_{-i\infty}^{i\infty} e^{-x^\beta} e^{sx} dx \quad (\text{S36})$$

Changing $u = -ix$, Johnston shown that

$$P(s, \beta) = \frac{1}{\pi} \int_0^{\infty} e^{-u^\beta \cos(\pi\beta/2)} \cos [su - u^\beta \sin(\pi\beta/2)] du \quad (\text{S37})$$

which can be evaluated numerically. Some examples are provided in Fig. S12. It is important to notice that the maximum of the distribution is not directly related to the data extracted relaxation time T_1^{str} . However, Johnston has shown that that $\frac{1}{T_1^{\text{str}}}$ is not the average relaxation rate but rather a characteristic property of the probability distribution $P(s, \beta)$. Specifically, $\frac{1}{T_1^{\text{str}}}$ is the value such that relaxation rates $\frac{1}{T_1}$ are about equally likely to be less than $\frac{1}{T_1^{\text{str}}}$ as they are to be greater than $\frac{1}{T_1^{\text{str}}}$. This means $\frac{1}{T_1^{\text{str}}}$ can be interpreted as a median relaxation rate within the distribution of relaxation rates.

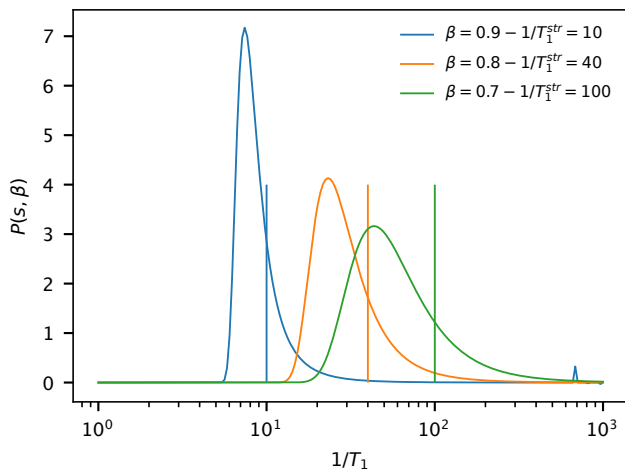


Figure S12. The probability density function, $P(s, \beta)$, which represents the distribution of relaxation rates (s), is shown for various stretched parameters: $\beta = 0.9$ with $1/T_{\text{str}} = 10 \text{ s}^{-1}$; $\beta = 0.8$ with $1/T_{\text{str}} = 40 \text{ s}^{-1}$; and $\beta = 0.7$ with $1/T_{\text{str}} = 100 \text{ s}^{-1}$. $P(s, \beta)$ was computed using Equation ((S37)), illustrating how different values of β and $1/T_{\text{str}}$ correspond to different distributions. A vertical line marks the input value of $1/T_{\text{str}}$ for each set of parameters to guide the eye.

DFT CALCULATIONS

Computational details

Theoretical calculations were based on the Density Functional Theory (DFT) and were performed using the ORCA 6.0 program.^[1,2] To facilitate comparison between theory and experiment, the X-ray crystal structure of (o-DMTTF)₂ was used. The DFT model includes two dimethyltetraphthalifulvalene units together with 6 bromine counter-ions. The hydrogen atoms of the DFT model were geometry-optimized while constraining the positions of other atoms to their experimentally derived coordinates. All calculations were carried out using the hybrid functional B3LYP^[3,4] and the x2c-TZVPall basis sets.^[5] Relativistic effects were included using the exact two-component (X2C) Hamiltonian.^[6-8] Tight convergence criteria were imposed using the TightSCF keyword along with the default (DefGrid2) integration grids. Dispersion correction was applied according to the method developed by Grimme with the Becke-Johnson damping scheme (D3BJ).^[9] The spin-orbit coupling (SOC) operator was treated by a mean-field approximation to the Breitâ€¢Pauli operator (SOCType 3 in ORCA).^[10] Construction of the effective potential included one-electron terms, the Coulomb term was computed with the RI approximation, exchange was incorporated via one-center exact integrals including spin-other orbit interactions, and local DFT correlation was included with VWN5 (all these choices are set with the keyword "SOCFlags 1,3,3,1" in ORCA).

Computational results

References

- [1] F. Neese *Wiley Interdiscip. Rev.: Comput. Mol. Sci.* **8**, 1 (2018).
- [2] F. Neese, *WIREs Comput. Mol. Sci.* **12**, e1606, (2022).
- [3] A.D. Becke, *J. Chem. Phys.* **98**, 1372â€¢1377 (1993).
- [4] C. Lee, W. Yang, R.G. Parr, *Phys. Rev. B* **37**, 785â€¢789 (1988).
- [5] P. Pollak, F. Weigend, *J. Chem. Theory Comput.* **13**, 3696-3705 (2017).
- [6] D. Peng, N. Middendorf, F. Weigend, M. Reiher, *J. Chem. Phys.* **138**, 184105 (2013).
- [7] Y. J. Franzke, N. Middendorf, F. Weigend, *J. Chem. Phys.* **148**, 104110 (2018).
- [8] Y. J. Franzke, J. M. Yu, *J. Chem. Theory Comput.* **18**, 323-343 (2022).
- [9] S. Grimme, J. Antony, S. Ehrlich, H. A. Krieg *J. Chem. Phys.* **132**, 154104 (2010).
- [10] S. Grimme, S. Ehrlich, L. Goerigk, *J. Comput. Chem.* **32**, 1456â€¢1465 (2011).
- [11] F. Neese, *J. Chem. Phys.* **122**, 034107 (2005).

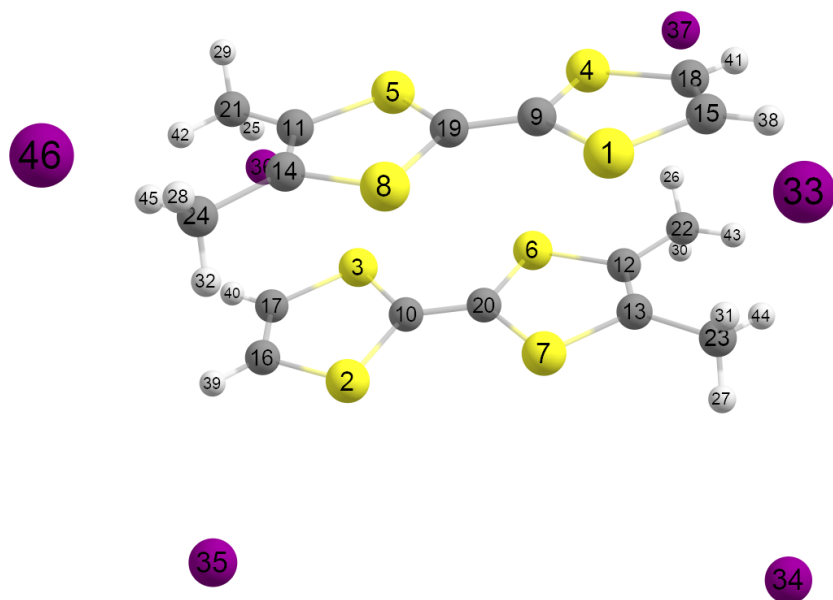


Figure S13. Atom labelling of the DFT model for $(o\text{-DMTTF})_2\text{I}$

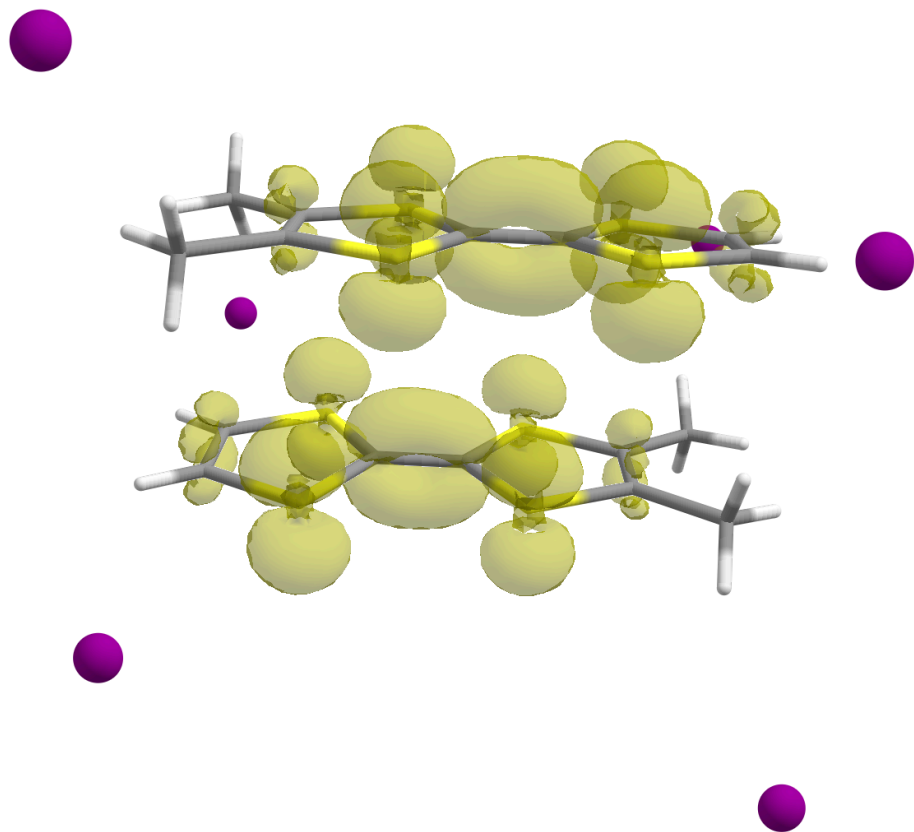


Figure S14. DFT-computed spin density plot of $(o\text{-DMTTF})_2\text{I}$

Table S2. DFT-computed hyperfine coupling constants (total values A_{ii} , and individual spin-dipolar components A_{ii}^{SD} , in MHz for $(o\text{-DMTTF})_2\text{I}$

Center	A_{11}	A_{11}^{SD}	A_{22}	A_{22}^{SD}	A_{33}	A_{33}^{SD}	A_{iso}
H25	1.23	-0.74	1.74	-0.23	2.95	0.97	1.97
H29	1.04	-0.55	1.16	-0.42	2.58	0.98	1.59
H42	-0.38	-0.30	-0.73	-0.64	0.87	0.95	-0.08
H28	0.09	-0.52	0.25	-0.37	1.53	0.89	0.62
H32	0.54	-0.71	1.09	-0.17	2.15	0.88	1.26
H45	-0.25	-0.30	-0.50	-0.55	0.90	0.85	0.05
H38	0.44	1.66	-1.83	-0.53	-2.41	-1.13	-1.26
H41	0.25	1.83	-1.99	-0.37	-3.09	-1.46	-1.61
H39	0.44	1.66	-1.83	-0.53	-2.41	-1.13	-1.26
H40	0.25	1.83	-1.99	-0.37	-3.09	-1.46	-1.61
H26	1.23	-0.74	1.74	-0.23	2.95	0.97	1.97
H30	1.04	-0.55	1.16	-0.42	2.58	0.98	1.59
H43	-0.38	-0.30	-0.72	-0.64	0.87	0.95	-0.08
H27	0.09	-0.52	0.25	-0.37	1.53	0.89	0.62
H31	0.54	-0.71	1.09	-0.17	2.15	0.88	1.26
H44	-0.25	-0.30	-0.50	-0.55	0.90	0.85	0.05